Reliability of resting-state functional connectivity in the human spinal cord: assessing the impact of distinct noise sources

Merve Kaptan [a*], Ulrike Horn [a], S. Johanna Vannesjo [b], Toralf Mildner [c], Nikolaus Weiskopf [d,e], Jürgen Finsterbusch [f], Jonathan C.W. Brooks [g], Falk Eippert [a*]

[a] Max Planck Research Group Pain Perception, Max Planck Institute for Human Cognitive and Brain Sciences, Leipzig, Germany

[b] Department of Physics, Norwegian University of Science and Technology, Trondheim, Norway

[c] Methods & Development Group Nuclear Magnetic Resonance, Max Planck Institute for Human Cognitive and Brain Sciences, Leipzig, Germany

[d] Department of Neurophysics, Max Planck Institute for Human Cognitive and Brain Sciences, Leipzig, Germany

[e] Felix Bloch Institute for Solid State Physics, Faculty of Physics and Earth Sciences, University of Leipzig, Leipzig, Germany

[f] Department of Systems Neuroscience, University Medical Center Hamburg-Eppendorf, Hamburg, Germany

[g] School of Psychology, University of East Anglia Wellcome Wolfson Brain Imaging Centre (UWWBIC), Norwich, United Kingdom

[*] Corresponding authors

Address for correspondence: Merve Kaptan & Falk Eippert; Max Planck Research Group Pain Perception, Max Planck Institute for Human Cognitive and Brain Sciences, Stephanstraße 1a, 04103 Leipzig, Germany, Phone: +49 341 9940 2224; mkaptan@stanford.edu; eippert@cbs.mpg.de

Acknowledgments: The authors would like to thank Alice Dabbagh for helpful discussions on fMRI reliability, the radiographers at MPI CBS for invaluable help with data acquisition and all volunteers for taking part in this study, as well as Benjamin Ades-Aron and Paul Taylor for help with MP-PCA and 3dFWHMx implementation, respectively.

Abstract

The investigation of spontaneous fluctuations of the blood-oxygen-level-dependent (BOLD) signal has recently been extended from the brain to the spinal cord, where it has also generated initial interest from a clinical perspective. A number of resting-state functional magnetic resonance imaging (fMRI) studies have demonstrated robust functional connectivity between the time-series of BOLD fluctuations in bilateral dorsal horns and between those in bilateral ventral horns, in line with the functional neuroanatomy of the spinal cord. A necessary step prior to extension to clinical studies is assessing the reliability of such resting-state signals, which we aimed to do here in a group of 45 healthy young adults at the clinically prevalent field-strength of 3T. When investigating connectivity in the entire cervical spinal cord, we observed fair to good reliability for dorsal-dorsal and ventral-ventral connectivity, whereas reliability was poor for within- and between-hemicord dorsal-ventral connectivity. Considering how prone spinal cord fMRI is to noise, we extensively investigated the impact of distinct noise sources and made two crucial observations: removal of physiological noise led to a reduction in functional connectivity strength and reliability – due to the removal of stable and participant-specific noise patterns – whereas removal of thermal noise considerably increased the detectability of functional connectivity without a clear influence on reliability. Finally, we also assessed connectivity within spinal cord segments and observed that while the pattern of connectivity was similar to that of whole cervical cord, reliability at the level of single segments was consistently poor. Taken together, our results demonstrate the presence of reliable resting-state functional connectivity in the human spinal cord even after thoroughly accounting for physiological and thermal noise, but at the same time urge caution if focal changes in connectivity (e.g. due to segmental lesions) are to be studied, especially in a longitudinal manner.

1. Introduction

Over the last decades, the spatiotemporal organization of spontaneous fluctuations of BOLD signals in the brain has been widely investigated and intrinsic resting-state networks have been considered as building blocks of brain function that are relevant for cognition and behavior (Deco et al., 2011; Fox & Raichle, 2007; Petersen & Sporns, 2015; Raichle et al., 2001; Wig, 2017). With a delay of about 20 years and on a much smaller scale, a similar perspective has opened up for spinal cord function, with resting-state fMRI studies demonstrating that spontaneous BOLD fluctuations of the spinal cord are spatiotemporally organized as well (Barry et al., 2014; Barry et al., 2016; Barry et al., 2018; Conrad et al., 2018; Eippert et al., 2017a; Harita & Stroman, 2017; Harita et al., 2018; Hu et al., 2018; Ioachim et al., 2019; Ioachim et al., 2020; Kinany et al., 2020; Kong et al., 2014; Liu et al., 2016a; Liu et al., 2016b; Martucci et al., 2019; Martucci et al., 2021; San Emeterio Nateras et al., 2016; Vahdat et al., 2020; Weber et al., 2018; Wei et al., 2009; for a review see Harrison et al., 2021). More specifically, region-of-interest (ROI) based functional connectivity techniques have revealed statistically significant connectivity between the time-series of bilateral ventral horns as well as between bilateral dorsal horns in humans and similar functional connectivity patterns have been identified in non-human primates and rodents as well (Chen et al., 2015; Wu et al., 2018; Wu et al., 2019). Since the dorsal horns receive somatosensory information from the body and the ventral horns contain cell bodies of the motor neurons (Hochman, 2007), the observed connectivity patterns appear to be well aligned with the spinal cord's functional organization.

Resting-state fMRI metrics are often considered in the context of biomarker development (Hohenfeld et al., 2018; Parkes et al., 2018; Pfannmöller & Lotze, 2019), i.e. for monitoring and prediction of disease progression or treatment response. This approach could obviously be extended towards the spinal cord as well (e.g. in the context of recovery after spinal cord injury) and first steps have already been taken in this direction by assessing changes in spinal cord resting-state connectivity in sensory and motor disorders with diffuse or localized spinal pathology (Chen et al., 2015; Combes et al., 2022; Conrad et al., 2018; Martucci et al., 2019). However, before the clinical utility of resting-state metrics can be established, a necessary first step is to assess their reliability as well as the factors that influence it. In this respect, it is important to note that only a very limited number of studies have investigated the test-retest reliability (i.e., the stability of a measure under repeated measures; Shrout and Fleiss, 1979; Shrout and Lane, 2012) of resting-state networks in the human spinal cord: only one study at 7T (Barry et al. 2016) and four studies at the clinically-relevant field strength of 3T (Barry et al., 2018; San Emeterio Nateras et al., 2016; Liu et al., 2016; Hu et al., 2018), though these latter ones had rather small sample sizes (N=1 and N=10).

These studies provided an initial assessment of test-retest reliability, but did not investigate the factors that might shape reliability in-depth. Given the susceptibility of spinal cord fMRI to the detrimental influence of noise (Cohen-Adad et al., 2010; for review, see Fratini et al., 2014; Eippert et al., 2017b), it is however essential to understand how distinct noise sources might impact spinal cord resting-state functional connectivity and its reliability – a relationship that, even in the brain, is not necessarily straightforward (Birn et al., 2014; Noble et al., 2019; Shirer et al., 2015). A first noise source of relevance is physiological noise of cardiac and respiratory origin, to which spinal cord fMRI is especially prone (Harita & Stroman, 2017; Piché et al.,

2009; Verma & Cohen-Adad, 2014). Physiological noise of structured nature is particularly detrimental for resting-state fMRI studies as one cannot explicitly model the intrinsic activity of interest (unlike in task-based fMRI), which makes it more challenging to attribute the observed results to the underlying neuronal activity instead of non-neural confounds (Birn, 2012; Birn et al., 2014; Murphy et al., 2013). Another major source of noise that influences fMRI measurements is thermal noise (Edelstein et al., 1986; Hoult & Richards, 1976), which has not been investigated in the context of spinal cord fMRI to our knowledge. While thermal noise – whose principal source is the thermal fluctuations within the subject that is imaged, followed by noise due to scanner electronics – is not structured, its removal may further benefit the detectability of BOLD signals of interest (Ades-Aron et al., 2021a; Adhikari et al., 2019; Vizioli et al., 2021).

Considering all the above, the aims of the current study are as follows. First, we aim to replicate previous resting-state fMRI functional connectivity results and assess their test-retest reliability in a large sample (N=45) at the clinically-relevant field strength of 3T across the entire cervical spinal cord. Second, we aim to assess how structured (physiological) and unstructured (thermal) noise sources impact functional connectivity and its reliability. Finally, we aim to investigate more localized aspects of functional connectivity and its reliability, namely within each spinal cord segment, i.e. the macro-scale building blocks of spinal cord organization.

2. Methods

2.1. Participants

This study is based on the participant sample of Kaptan et al. (2022), which contained data from 48 healthy participants. As our focus in the current study was on assessing the influence of different noise sources on the reliability of resting-state functional connectivity, data from three participants had to be discarded due to technical problems in the acquisition of peripheral physiological data (i.e., corrupted ECG-recordings), thus leading to a final sample size of 45 participants (20 females, age: 27 ± 3.8). All participants provided written informed consent and the study was approved by the Ethics Committee at the Medical Faculty of the University of Leipzig.

2.2. Data acquisition

All measurements were performed on a 3T whole-body Siemens Prisma MRI System (Siemens, Erlangen, Germany) equipped with a whole-body radio-frequency (RF) transmit coil, a 64-channel RF head-and-neck coil, and a 32-channel RF spine-array, using the head coil element groups 5–7, the neck coil element groups 1 and 2, and spine coil element group 1 (all receive-only). Before the start of data acquisition, typical instructions for spinal MRI studies were given to the participants (i.e., they were told not to move, to avoid excessive swallowing and to breathe normally; see Cohen-Adad et al., 2021). The here-described data are part of a larger methodological project: we thus only describe the relevant parts – two functional acquisitions and one structural acquisition – and refer the interested reader to the methodological publication for further details on this dataset (Kaptan et al., 2022).

Functional runs consisted of 250 single-shot 2D gradient-echo EPI volumes (acquisition time: ~10min) that covered the spinal cord from the 2nd cervical vertebra to the 1st thoracic vertebra and were acquired with the following parameters: slice orientation: transverse oblique; number of slices: 24; slice thickness: 5.0mm; field of view: 128×128mm^2, in-plane resolution: 1.0 × 1.0mm^2; TR: 2312ms; TE: 40ms; excitation flip angle: 84°, GRAPPA acceleration factor: 2; partial Fourier factor: 7/8; phase-encoding direction: anterior-to-posterior; echo spacing: 0.93ms; bandwidth per pixel: 1220 Hz/Pixel. Both functional runs employed slice-specific z-shimming (Finsterbusch et al., 2012) in order to overcome the signal-loss that occurs due to local magnetic field inhomogeneities. The two runs only differed according to the selection method of slice-specific z-shims: this occurred either manually or automatically (Kaptan et al., 2022). The two runs were separated from each other by a maximum of ~10 minutes, did not show a systematic order difference (the run with manual selection of z-shims occurred before the run with automatic selection of z-shims in 23 of the 45 participants) and exhibited highly similar gray matter tSNR (run with manual selection of z-shims: 15.7 ± 1.3; run with automatic selection of z-shims: 15.4 ± 1.3; mean ± standard deviation). During each of the runs, participants were presented with a white cross-hair on a gray background, which they were asked to fixate on.

Additionally, a high-resolution T2-weighted acquisition (3D sagittal SPACE sequence, Cohen-Adad et al., 2021; 64 sagittal slices; resolution: 0.8×0.8×0.8mm^3; field-of-view: 256×256mm^2;

158 TE: 120ms; flip angle: 120°; TR: 1500ms; GRAPPA acceleration factor: 3; acquisition time:
159 4.02min) was obtained for registration purposes.

160 During fMRI data acquisition, we also acquired peripheral physiological signals in order to
161 perform physiological noise modelling: respiratory data were acquired via a breathing belt and
162 cardiac data were acquired via ECG electrodes (BrainAmp ExG system; Brain Products GmbH,
163 Gilching, Germany). Data acquisition occurred with a sampling-rate of 1kHz and included
164 scanner triggers to allow for synchronization of data streams.

165

166 **2.3. Data preprocessing**

167 Preprocessing steps were performed using MATLAB (version 2021a), EEGLAB (version
168 2019.0; Delorme & Makeig, 2004), FMRIB Software Library (FSL; version 6.0.3; Jenkinson
169 et al., 2012), and Spinal Cord Toolbox (SCT; version 4.2.2; De Leener et al., 2017).

170

171 **2.3.1. Preprocessing of physiological data**

172 ECG data were processed within EEGLAB (Delorme & Makeig, 2004) using the FMRIB plug-
173 in (https://fsl.fmrib.ox.ac.uk/eeglab/fmribplugin/). This algorithm allows for the correction of
174 gradient artifacts in the ECG signal caused by the switching of magnetic gradients during fMRI
175 acquisitions (Niazy et al., 2005). R-peaks were automatically detected after correction and
176 where necessary manual corrections were carried out using in-house MATLAB scripts.

177 We calculated the heart-period (i.e., R-R interval) in milliseconds as the average difference in
178 time between each R peak for each functional run. In addition to that, we assessed heart-period
179 variability by calculating the standard deviation of R-R intervals (Shaffer & Ginsberg, 2017)
180 within each of the two functional runs.

181 The respiratory period was calculated as described by Bach and colleagues (2016). More
182 specifically, the respiration traces were i) mean-centered, ii) filtered with a band pass filter
183 (cut-off frequencies: 0.01 Hz and 0.6 Hz), and iii) median filtered over 1s. The start of
184 inspiration was defined as a negative zero-crossing. After each detected cycle, a 1s refractory
185 period was imposed, to account for residual signal noise that may lead to the occurrence of
186 several zero-crossings on the same respiratory cycle (Bach et al., 2016). We report the mean
187 and standard deviation of the respiratory period in seconds.

188

189 **2.3.2. Preprocessing of fMRI data**
190 **2.3.2.1. Motion-correction**

191 For each functional run, a slice-wise motion correction procedure with regularization in z-
192 direction (as implemented in SCT, "*sct_fmri_moco*") was employed in two steps. First, the 250
193 volumes of each run were averaged to create a mean image, and this mean image was used to
194 automatically determine the centerline of the cord. A cylindrical mask (with a diameter of
195 41mm) was generated based on this centerline and used during the motion-correction procedure
196 to ensure that regions moving independently from the cord would not adversely impact the

motion-correction. The previously-created mean image was used as a target for the first iteration of slice-wise motion correction with a 2nd degree polynomial and spline interpolation. In the second step, the mean of motion-corrected time-series from the first step served as a target image for the second iteration of motion-correction, which was applied to the raw images (with the same algorithm parameters).

2.3.2.2. Segmentation

For the functional runs, binary masks/segmentations of the spinal cord were manually created based on each mean image after motion-correction. We employed a manual segmentation instead of an automated segmentation to ensure that the segmentation quality did not adversely affect the registration procedure (see below), which was dependent on the segmentation.

Binary masks/segmentations of the spinal cord obtained from the T2-weighted images were created automatically using the '*sct_deepseg*' approach of SCT (Gros et al., 2019).

2.3.2.3. Registration

Functional connectivity analyses were performed in native space to make them comparable to those of a previous study on resting-state functional connectivity and its reliability by Barry and colleagues (2016). However, a registration procedure to the PAM50 template space (De Leener et al., 2018) was still performed in order to obtain the warping fields that allowed to bring region-specific probabilistic masks from PAM50 template space to each individual's native space ('*sct_warp_template'*).

First, anatomical T2-weighted images were normalized to the template space with the following three consecutive steps (*'sct_register_to_template'*): i) the spinal cord was straightened using the binary cord segmentation, ii) the automatically labelled C2-C7 vertebral levels (created via '*sct_label_vertebrae*', with manual corrections when deemed necessary) were used for the vertebral alignment between the template and the anatomical images, iii) the anatomical images were registered to the template using non-rigid segmentation-based transformations.

Second, the T2-weighted PAM50 template was registered to the mean of motion-corrected functional images using non-rigid transformations ('*sct_register_multimodal*'; with the initial step using the inverse warping field obtained from the registration of the T2-weighted anatomical image to the template image). The resulting warping fields obtained from this registration were then applied to the PAM50 probabilistic gray matter and segmental level masks to bring them into the native space where connectivity estimation and statistical analyses were carried out.

2.3.3. Denoising

As we aimed to investigate the effect of various noise sources on resting-state functional connectivity and its reliability, we employed different denoising pipelines to assess the impact of specific noise sources.

2.3.3.1. Physiological noise

First, we employed a processing pipeline that does not explicitly account for any specific noise source – from now on we refer to this pipeline as '*baseline*' throughout the manuscript. The baseline denoising pipeline consisted of i) motion-correction, ii) high-pass filtering (with a 100s cut-off), and iii) "motion-censoring". Censoring was necessary to ensure that outlier volumes that were either inadvertently introduced by the motion-correction algorithm or that occurred due to a sudden large movement of participants did not artificially inflate the connectivity estimates (as outlier volumes can create spikes in the signal time-series of ROIs). The outlier volumes were determined using the dVARS (the root mean square difference between successive volumes; Smyser et al., 2011) and refRMS (root mean square intensity difference of each volume to the reference volume) metrics as implemented in the '*fsl_motion_outliers'* function of FSL. Volumes presenting with dVARS or refRMS values two standard deviations above the mean values of each run were selected as outliers. In the later occurring GLM estimation, these outlier volumes were modelled as individual regressors (on average, 4.67 ± 3.15 volumes were identified as outliers across all participants and sessions, i.e. less than 2% of the volumes).

Second, physiological noise modelling (PNM; Brooks et al., 2008) was used to obtain slice-specific regressors to account for physiological confounds. PNM is a modification of the RETROICOR approach (Glover et al., 2000) and creates slice-specific regressors via calculating their phase for each slice relative to the cardiac and respiratory cycles by modelling them via Fourier basis series with a combination of sine and cosine harmonics (Brooks et al., 2008; Kong et al., 2012). We utilized regressors up to the fourth harmonic – resulting in a total of 16 regressors – to account for cardiac and respiratory processes, and another 16 regressors to account for their interactions, resulting in a total of 32 regressors (Brooks et al., 2008; Kong et al., 2012). In addition to that, a slice-specific CSF regressor was created (as implemented in PNM) by extracting the signal from the voxels whose variance were in the top 10 percentile within a region including both the spinal cord and CSF space. Note that all noise regressors were high-pass filtered with the same 100s cut-off prior to noise regression to prevent spectral misspecification (Hallquist et al., 2013).

Third, a specific set of regressors that account for different physiological noise sources was then added to the baseline denoising pipeline, and regressed out from the functional data using FEAT (FMRI Expert Analysis Tool; http://fsl.fmrib.ox.ac.uk/fsl/fslwiki/FEAT), resulting in the seven different denoising pipelines listed below:

i. Baseline (consisting of motion-correction, high-pass filtering and censoring)

ii. Baseline + slice-specific motion-correction estimates (x- and y- translation; automatically obtained from the slice-wise motion correction procedure)

iii. Baseline + CSF signal

iv. Baseline + eight respiratory regressors

v. Baseline + eight cardiac regressors

vi. Baseline + thirty-two PNM regressors (including eight respiratory regressors, eight cardiac regressors, and 16 interaction regressors)

vii. Maximal (motion-correction, high-pass filtering, censoring, slice-specific motion correction regressors, 32 PNM regressors and a CSF regressor)

The residuals obtained from each of the denoising pipelines were then used for further analysis. Please note that while we did not include a pre-whitening step in our above-mentioned denoising pipelines, we assessed the impact of pre-whitening carried out using FILM (FMRIB's Improved Linear Model with local autocorrelation correction; Woolrich et al., 2001) by comparing maximal denoising with maximal denoising + FILM pre-whitening (see Table S1).

2.3.3.2. Thermal noise

Another major source of noise that contributes to the variability of fMRI time-series is zero-mean Gaussian thermal noise which arises from thermal fluctuations within the participant, as well as scanner electronics (Edelstein et al., 1986; Hoult & Richards, 1976). Here, we employed two different approaches to address the influence of thermal noise: spatial smoothing and denoising based on Marchenko-Pastur Principle Component Analysis (MP-PCA; Marčenko & Pastur, 1967; Veraart et al., 2016a; Veraart et al., 2016b), either of which was employed before GLM-based physiological noise correction via the maximal denoising pipeline was carried out. Spatial smoothing was implemented in FEAT with isotropic Gaussian kernels of either 2mm or 4mm FWHM. Non-local MP-PCA was implemented using an openly available MATLAB algorithm (http://github.com/NYU-DiffusionMRI/mppca_denoise; Ades-Aron et al., 2021b) and was applied to the entire fMRI time-series data (dimensions [x, y, z, time]: 128 × 128 × 24 × 250) before motion correction. In the context of MRI, MP-PCA was originally evaluated for thermal noise reduction in diffusion MRI data (Veraart et al., 2016a; Veraart et al., 2016b), but has recently also been applied to task-based (Ades-Aron et al., 2021a) and resting-state (Adhikari et al., 2019) fMRI data of the brain, aiming to minimize the contributions of thermal noise to fMRI time series without altering the spatial resolution.

Finally, in order to estimate the effect of thermal noise removal – via smoothing or MP-PCA – on the data's spatial smoothness, we estimated the spatial autocorrelation function of the residuals after each of four processing pipelines (maximal, maximal + MP-PCA, maximal + smoothing 2mm, maximal + smoothing 4mm) using the 3dFWHMx function of AFNI (Cox et al., 2017). The smoothness estimates were derived from AFNI's mixed gaussian and mono-exponential decay model and we report the effective (combined) smoothness value after each denoising approach (already incorporating smoothness changes introduced during motion correction).

2.4. Statistical analysis

2.4.1. Functional connectivity calculation

Functional connectivity was assessed using an ROI-based approach. The ROI masks were created using the probabilistic PAM50 gray matter masks that were warped from template space to the native space of each participant (see section 2.3.2.3). In native space, the probabilistic gray matter masks were thresholded at 70% for each slice separately to ensure that there were no voxels shared between distinct ROIs. Within a slice, the ROIs typically contained 1.6 and 1.5 voxels in the left and right dorsal horns, and 1.9 and 1.9 voxels in the left and right ventral horns, respectively (average over slices and participants). *Slice-specific* time courses were then extracted via averaging the signal over the voxels within each of the four ROIs (left dorsal horn, left ventral horn, right dorsal horn, and right ventral horn).

Next, slice-wise correlations between ROIs were calculated using the Pearson correlation coefficient. In order to address the effects of any remaining global signal fluctuations that might be shared between the ROIs (e.g. residual movement or physiological noise effects) we also calculated partial correlation coefficients (see Figure S1). The dorsal-ventral correlations within each hemicord (left dorsal with left ventral and right dorsal with right ventral), as well as between hemicords (left dorsal with right ventral and right dorsal with left ventral) were averaged, yielding one within-hemicord and one between-hemicord dorsal-ventral connectivity value for each participant (similar to Eippert et al. 2017a, who did not observe any significant laterality differences). The slice-wise correlation coefficients were then averaged over all slices along the superior-inferior axis of the cord, yielding four functional connectivity estimates for each participant: dorsal-dorsal, ventral-ventral, dorsal-ventral within-hemicord and dorsal-ventral between-hemicord. This averaging of correlation values might lead to a slight conservative bias in our results as we did not perform Fischer's z-transformation prior to averaging, however, this is assumed to be negligible (Silver & Dunlap, 1987; Corey et al., 1998; Eippert et al., 2017a). Note that only those slices that were assigned to C3-T1 probabilistic segmental levels were included, resulting in a variable number of slices across different participants due to the anatomy of the participants (depending on the coverage of the EPI slice-stack during acquisition). At the group-level, we report the mean r value, i.e. averaged across two sessions and averaged across participants.

The significance of the functional connectivity estimates or the difference between them (depending on the aim of the analysis) were assessed using permutation-based tests implemented in the Permutation Analysis of Linear Models software (PALM; Winkler et al., 2014). The number of permutations was set to 10,000 and we report two-tailed family-wise error (FWE) corrected p-values (adjusted according to the number of tests performed).

2.4.1.1. Within-segment functional connectivity

In order to provide insights into the segment-wise organization of functional connectivity, we also investigated the functional connectivity within each spinal segment covered by our imaging volume; those included all segments between the third cervical (C3) and first thoracic segment (T1). Therefore, probabilistic segmental levels from PAM50 template space were first

warped to each participant's native space (see section 2.3.2.3). Then, to guarantee that there was no overlap between neighboring segments, the slice with the highest probability of belonging to a specific segmental level and the slice above and below were assigned to the corresponding segment. This procedure ensured that there were a similar number of slices for each segment and led to a 15 mm segment length, which is in line with empirical measurements of cervical segment length based on post-mortem data (Ko et al., 2004). Slice-wise functional connectivity was calculated as described above and the correlation values for slices within each segment were averaged. The connectivity strength for each segment was tested against 0 via permutation tests as described above (see section 2.4.1). Please note that for all within-segment analyses, we used data that had undergone the maximal denoising pipeline for physiological noise correction and were also corrected for thermal noise via MP-PCA, as our whole-cord analyses had suggested that this was the optimal processing pipeline.

2.4.2. tSNR and explained variance

In order to provide further insights into the effects of the removal of various noise sources, we also calculated the gray matter temporal signal-to-noise ratio (tSNR) and the explained variance of the gray-matter time-series *for each denoising step* (please note that motion correction, high-pass filtering and motion-censoring was always performed). Voxelwise gray-matter tSNR values were calculated for each functional run via dividing each voxel's temporal mean by its temporal standard deviation (Parrish et al., 2000). The impact of various noise sources on gray-matter tSNR was assessed by comparing the tSNR values obtained after each denoising pipeline to the baseline denoising procedure – in addition to reporting descriptive values (% change) we also employed permutation-based tests as described above (see section 2.4.1) and report FWE-corrected p-values. Following Birn et al. (2014), the variance of gray-matter time-series explained by each denoising pipeline (R^2) was calculated by computing the fractional reduction in signal variance. tSNR and explained variance for each gray matter region were extracted using the native-space thresholded and binarized PAM50 gray matter masks that were also used to calculate functional connectivity.

2.4.3. Estimation of reliability

The central aspect of this manuscript concerns the reliability of resting-state functional connectivity in the human spinal cord. While different fields have come to rely on different operationalizations of reliability (for an in-depth discussion, see Brandmaier et al., 2018), we here follow the tradition in resting-state functional connectivity research and employ the intra-class correlation coefficient (ICC) for assessing reliability (see also Noble et al., 2020). Considering that spinal cord fMRI is severely impacted by different noise sources, our reliability investigation was not only focused on the connectivity metrics, but also possibly contributing factors. Thus, we calculated the test-retest reliability for each of the following aspects: i) functional connectivity, ii) tSNR, iii) motion metrics (DVARS, refRMS), iv) cardiac metrics (mean heart period, heart period variability), v) respiratory metrics (mean respiratory period, respiratory period variability), and vi) explained variance of gray matter time-series.

For each of these metrics, we first created a 45×2 (i.e. participants×sessions) matrix and then assessed the reliability using the 'Case 2' intraclass correlation coefficient (ICC(2,1); two-way random effects model; McGraw & Wong, 1996; Shrout & Fleiss, 1979); this is often also referred to as 'absolute agreement' (Molloy & Birn, 2014). ICC(2,1) is defined as the following:

$$\mathrm{ICC}(2,1) = \frac{\sigma^2_{between}}{\sigma^2_{between} + \sigma^2_{session} + \sigma^2_{error}}$$

Where $\sigma^2_{between}$ corresponds to the variance among persons (between participant) and $\sigma^2_{session}$ corresponds to the variance between sessions. Given its formula, the ICC shows what proportion of the total variance can be attributed to between-persons differences (Brandmaier et al., 2018; Noble et al., 2019).

We also aimed to provide an estimate of uncertainty, and thus calculated the 95% confidence interval (CI) of ICC values via non-parametric bootstrapping performed in MATLAB. Throughout the manuscript, ICC values are interpreted according to standard procedures: poor <0.4, fair 0.4–0.59, good 0.6–0.74, excellent ≥0.75 (Cicchetti & Sparrow, 1981; Hallgren, 2012).

2.5. Open science statement

All the code necessary to reproduce the reported results is available on GitHub (https://github.com/eippertlab/restingstate-reliability-spinalcord). The underlying data are available in BIDS-format via OpenNeuro (https://openneuro.org/datasets/ds004386 ; note that the dataset is currently only accessible to reviewers, but will be made publicly available when the manuscript is published). The intended data-sharing via OpenNeuro was mentioned in the Informed Consent Form signed by the participants and approved by the Ethics Committee at the Medical Faculty of the University of Leipzig.

3. Results

3.1. Replication and extension of previous resting-state functional connectivity results

Our first aim was to i) replicate previous ROI-based resting-state functional connectivity fMRI findings and ii) quantify the test-retest reliability of resting-state functional connectivity at 3T in human spinal cord. To this end, we assessed connectivity between the dorsal horns, between the ventral horns and between the within-hemicord dorsal and ventral horns as well as between-hemicord dorsal and ventral horns (Figure 1A). All connectivity estimations were carried out on data that were subjected to extensive correction for physiological noise (i.e. the 'maximal' denoising pipeline), as is typical in spinal fMRI. To control for non-specific factors, we explored tSNR differences between the different horns, but observed rather similar group-averaged gray-matter tSNR (even though the tSNR of ventral horns were slightly higher (6.8%) compared to the dorsal horns), with the range of variation across participants also being similar (Figure 1B).

We observed highly significant positive connectivity between the dorsal horns ($r = 0.03$; $t = 9.5$; $p < 0.001$) as well as between the ventral horns ($r = 0.05$; $t = 11.6$; $p < 0.001$) and were thus able to replicate previous findings. Additionally, we observed significant negative dorsal-ventral connectivity within hemicords ($r = -0.02$; $t = -10.7$; $p < 0.001$) and positive dorsal-ventral connectivity between hemicords ($r = 0.01$; $t = 6.7$; $p < 0.001$), but these were weaker than the dorsal and ventral connectivity (Figure 1C). With regards to the robustness of these results at the individual level, 100% of the participants exhibited positive dorsal-dorsal and ventral-ventral connectivity, while 98% of participants exhibited negative dorsal-ventral within-hemicord connectivity and 84% of participants demonstrated positive dorsal-ventral between-hemicord connectivity.

In terms of the reliability of these connectivity patterns, the ICC of dorsal-dorsal connectivity (0.59, CI: 0.46 – 0.74) and of ventral-ventral connectivity (0.63, CI: 0.44 – 0.79) was in the upper part of the fair and the lower part of the good range, respectively, whereas the reliability of within- and between-hemicord dorsal-ventral connectivity was clearly in the poor range (within-hemicord: 0.30, CI: 0.06 – 0.53 ; between-hemicord: 0.18, CI : -0.03 – 0.38; Figure 1D). Both connectivity amplitude and reliability were also assessed by i) replacing Pearson correlation with partial correlation (in order to account for the effects of any possibly remaining global signal fluctuations) and ii) adding a pre-whitening step during the GLM estimation (in order to account for the temporal autocorrelation of the BOLD data), but neither of these approaches led to a relevant change in the here-reported results (see Figure S1 and Table S1, respectively).

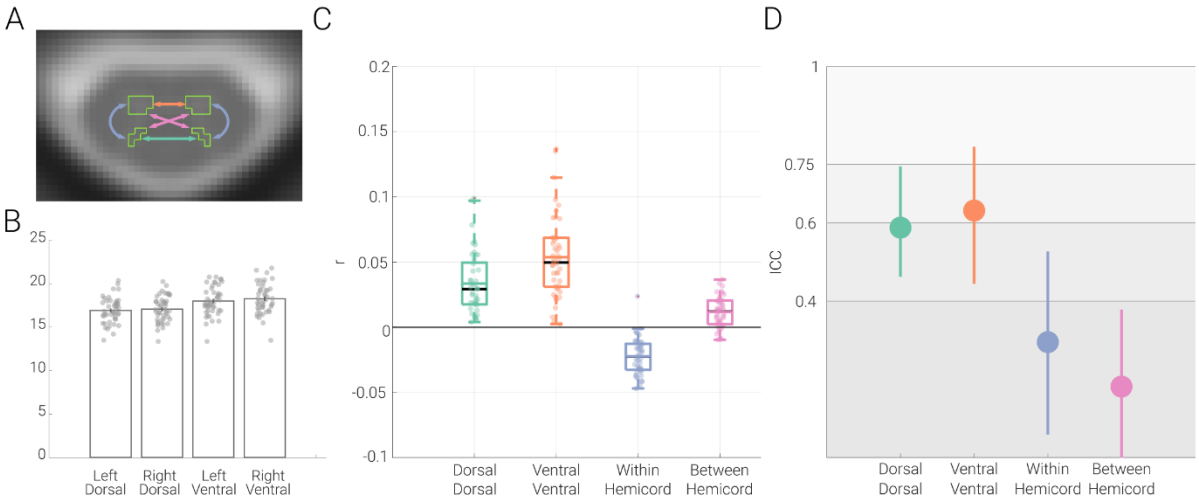

Figure 1. **Resting-state functional connectivity and its reliability. A. Functional connectivity calculation.** An exemplary transverse slice taken from the T2*-weighted PAM50 template (at segmental level C6) is shown with the gray matter masks overlaid as contours. The coloured arrows indicate the four different types of ROI-to-ROI connectivity that we investigated: dorsal-dorsal in green, ventral-ventral in orange, within-hemicord dorsal-ventral in blue, and between-hemicord dorsal-ventral in pink. **B. Gray matter tSNR.** Bar graphs show the tSNR for each of the gray matter ROIs. The vertical lines on the bars depict the standard error of the mean and the circles indicate participant-specific values. **C. Resting-state functional connectivity of the cervical cord.** Pearson correlation values (averaged across two sessions) between the time-courses of different ROIs are shown with box plots. For the box plots, the median is denoted by the black central line and the mean is denoted by the colored central line. The boxes represent the interquartile range and the whiskers encompass ~99% of the data. Correlation values from individual participants are shown with circles. **D. Test-retest reliability of resting-state connectivity.** ICC values for each connection are indicated via the circles, with the vertical lines representing the 95% confidence intervals. The gray scale background reflects the ICC ranges (as defined by Cicchetti & Sparrow (1981) and (Hallgren, 2012)): poor <0.4, fair 0.4–0.59, good 0.6–0.74, excellent ≥0.75.

3.2. Impact of noise sources on resting-state functional connectivity and its reliability

Considering that spinal cord fMRI is severely signal-to-noise limited due to the impact of various noise sources, we next investigated the relevance of each of these noise sources for the estimation of functional connectivity and its reliability. While the above-reported results were obtained after typical physiological noise correction procedures, we now separately assess physiological noise sources as well as thermal noise, which has hitherto been neglected in spinal cord fMRI. The effects of each noise source were evaluated by assessing the change in connectivity amplitude and reliability after it was removed.

3.2.1. Physiological noise and amplitude of functional connectivity

There are several general observations regarding the effects of physiological noise sources on functional connectivity (Figure 2; Tables 1 & 2). First, no matter which noise source was corrected for, the sign of the correlation stayed the same for all four connections and all four connections remained significant, indicating their robustness. Second, the (relatively weaker) within-hemicord and between-hemicord connectivity strength was not systematically impacted

by physiological noise correction. Third, and most importantly, dorsal-dorsal and ventral-ventral connections showed a consistent reduction in connectivity strength with increasingly stringent denoising. This latter point was also evident statistically, where a significant reduction in connectivity strength was observed for all noise sources, which became even more pronounced when combining the different noise regressors into combined sets (e.g. *PNM* pipeline and *maximal* pipeline; see Table 1). Interestingly, despite the strong reduction in correlation amplitude for dorsal-dorsal and ventral-ventral connections (of at least 50%) from the *baseline* to the *maximal* pipeline, the results remained clearly significant in the latter, which was likely due to the reduction in the inter-individual spread of amplitudes (i.e. higher precision). Supporting this overall pattern, highly similar results were obtained when Pearson correlation was replaced by partial correlation (Figure S1).

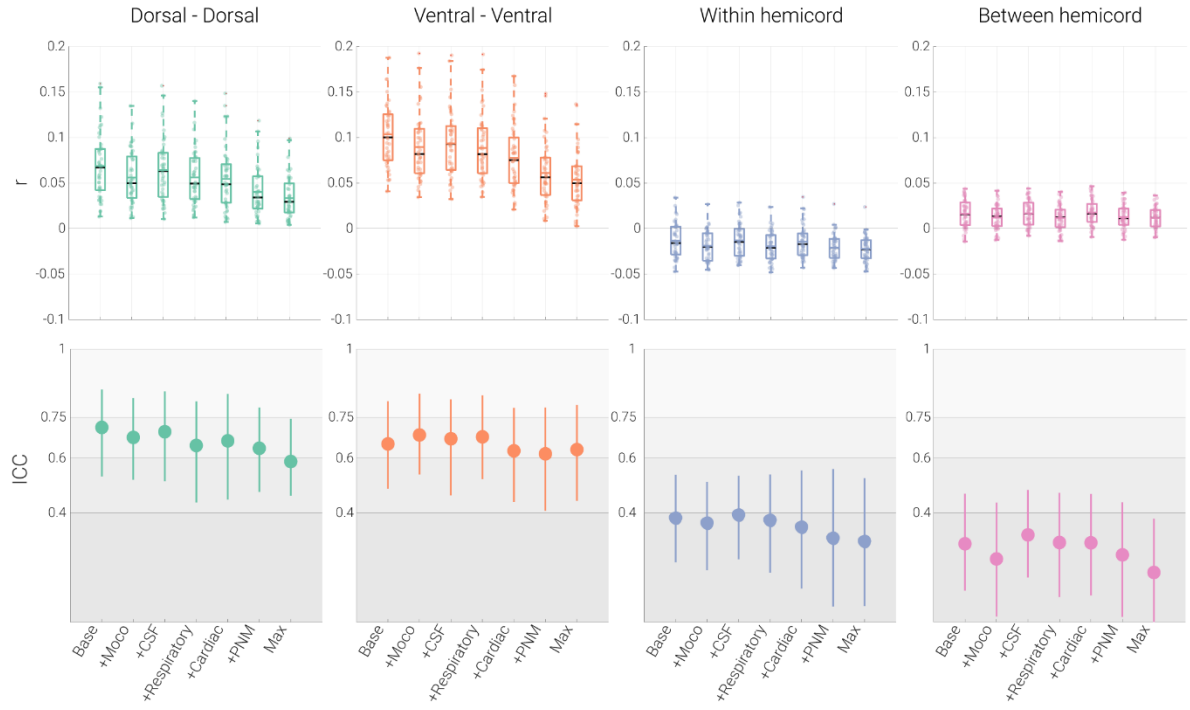

Figure 2. **Effects of physiological noise.** The top panel depicts Pearson correlation values (averaged within a participant across the two runs) between the time-courses of different ROIs via box plots for the seven denoising pipelines (Base: baseline processing; +Moco: baseline + slice-specific motion-correction estimates; +CSF: baseline + CSF signal; +Respiratory: baseline + eight respiratory regressors; +cardiac: baseline + eight cardiac regressors; +PNM: baseline + thirty-two PNM regressors; Max: baseline processing, slice-specific motion correction estimates, 32 PNM regressors and a CSF regressor). For the box plots, the median and mean are denoted by black and colored central lines, respectively. The boxes represent the interquartile range, with the whiskers encompassing ~99% of the data (outliers are denoted with red dots) and the circles representing individual participants. The bottom panel depicts ICC values for each the different pipelines via the circles, with the vertical lines representing the 95% confidence intervals. The gray scale background reflects the ICC ranges (as defined by Cicchetti & Sparrow (1981) and Hallgren (2012)): poor <0.4, fair 0.4–0.59, good 0.6–0.74, excellent ≥0.75.

3.2.2. Physiological noise and reliability of functional connectivity

Similar to the strength of functional connectivity, reliability also decreased with more stringent denoising (Figure 2; Table 1), though now for all four connections: the reliability of dorsal-dorsal connectivity decreased from good to fair (by 17.5%), the reliability of ventral-ventral functional connectivity stayed in the good range with a slight decline (by 3.19%), and the ICC values for within- and between-hemicord connectivity were consistently in the poor range, though with a clear decline of reliability being noticeable (22.5% and 36.7%, respectively). When looking at the influence of single noise sources, it becomes apparent that the strongest drop in reliability is observed due to removal of respiratory noise for dorsal-dorsal connectivity, whereas the removal of cardiac noise leads to the strongest decline of reliability in ventral-ventral connectivity.

The observed decrease in reliability may seem counter-intuitive at first glance, as the removal of physiological noise could be expected to increase reliability. However, such a pattern could arise if i) the noise is spatially structured (which is known to be the case for physiological noise) and ii) the processes that generate noise present with high reliability, which we set out to probe here. We noticed that metrics of motion (DVARS and refRMS), cardiac activity (mean heart period and heart period variability) and respiratory activity (mean respiratory period and respiratory period variability) not only strongly covaried across runs (Fig. 3A right panel), but also consistently exhibited excellent reliability, with ICCs between 0.75 and 0.94 (Fig. 3A left panel). Whether such a reliable noise-generating process also translates into a reliable influence on the measure of interest (i.e. gray matter time-series data) was investigated next.

Therefore, we assessed the effects of noise sources on tSNR (an often-used metric of fMRI time-series) and explained variance. With respect to gray matter tSNR changes (Figure 3B), the addition of the noise regressors led to the following increases: motion regressors 1.4%, CSF regressor 1.5%, respiratory regressors 2.9%, cardiac regressors 4.7%, PNM regressors 11.9%, and the combination of all regressors 13.4% (compared to the tSNR after the baseline pipeline), with all of increases significant at $p < 0.001$. Looking at this from the perspective of the fraction of gray-matter time-series variance explained by each of the noise regressors, we observed the following (Figure 3C right panel): motion regressors and the CSF regressor both 2.9%, respiratory and cardiac regressors 5.7% and 8.6%, PNM regressors 20.1% and combining all regressors 22.0%. Most importantly though, the variance explained by each of the noise components was highly reliable between runs (Figure 3C left panel): ICC values were mostly in the excellent range, varying between 0.73 to 0.89. Such a pattern of results is consistent with the above-mentioned reduction in amplitude and reliability of functional connectivity after denoising and provides evidence for the presence of structured and reliable non-neural signals being present in the gray-matter time-series.

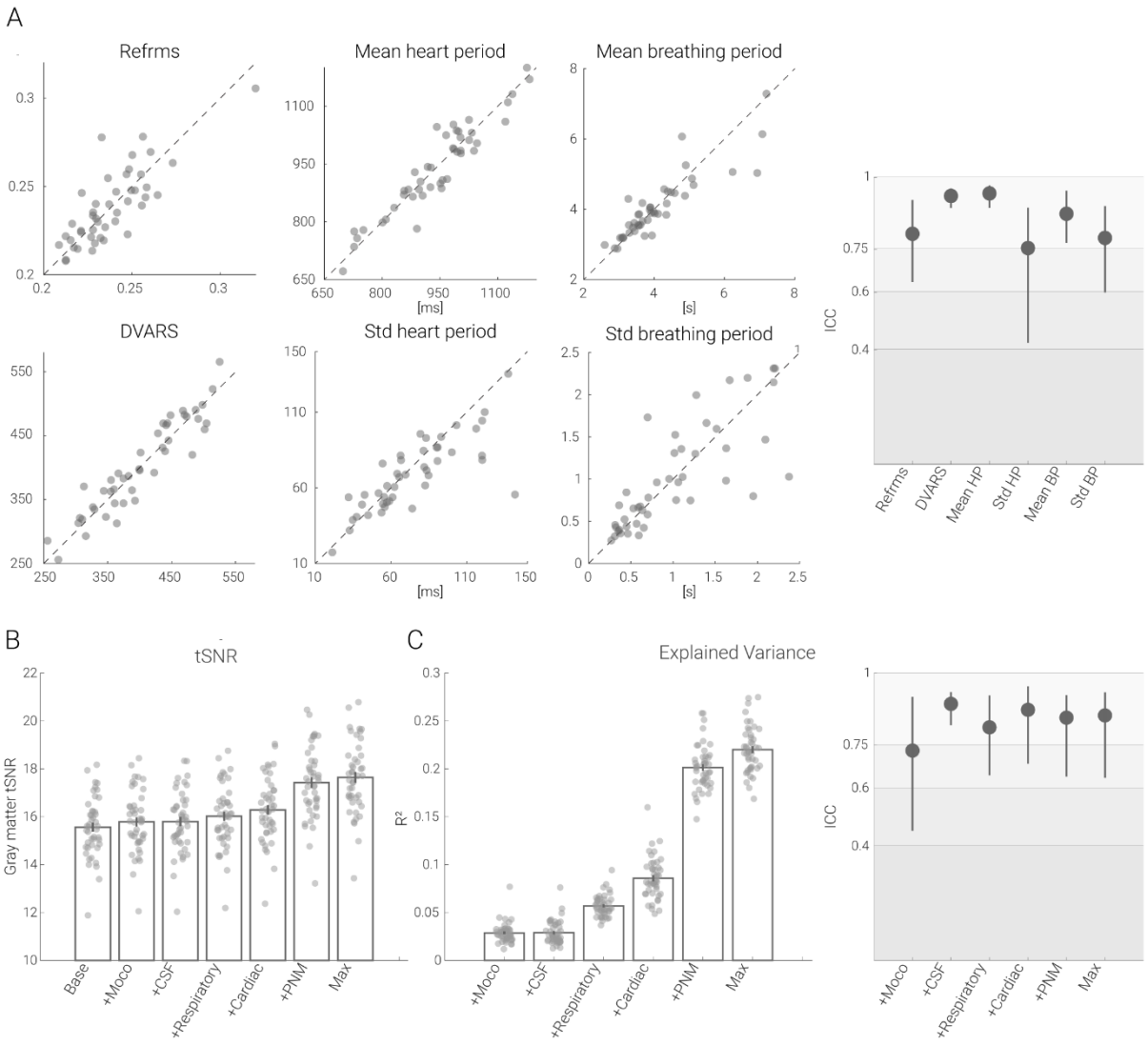

Figure 3. **Reliability of physiological measurements and effects on tSNR and explained variance in the gray matter. A.** Scatter plots show the metrics derived from physiological measurements recorded in each session, plotted against each other for every participant. On the very right, associated ICC values are depicted with the dots (lines depict 95% confidence intervals). **B.** Bar graphs show the gray matter tSNR after various physiological noise correction techniques have been applied. **C.** On the left, the bar graphs show the gray matter time-series variance accounted for by various physiological noise correction techniques. In all bar plots, the vertical lines on the bars depict the standard error of the mean and the circles indicate participant-specific values. On the right, ICC values for explained variance are shown with the filled circles and the lines depicting 95% confidence intervals. The gray scale background reflects the ICC ranges (as defined by Cicchetti & Sparrow (1981) and Hallgren (2012)): poor <0.4, fair 0.4–0.59, good 0.6–0.74, excellent ≥0.75.

3.2.3. Thermal noise

After having assessed the impact of physiological noise, we now turn our focus to the influence of thermal noise. We aimed to remove thermal noise either via MP-PCA or via spatial smoothing – both of these approaches were added to the maximal denoising pipeline for physiological noise (more specifically, they occurred before GLM-based physiological denoising), which now also served as the baseline to compare against.

Since thermal-noise removal has to our knowledge not been addressed in the spinal fMRI literature yet, we first assessed its impact on tSNR and observed a highly significant (all $p < 0.001$) increase in gray-matter tSNR after adding either MP-PCA (140.2%) or spatial smoothing with a 2mm (120.2%, $p < 0.001$) or 4mm kernel (260.4%, $p < 0.001$). This increase in tSNR was thus similar to what was observed when adding physiological noise correction regressors, though now of much stronger amplitude. In sharp contrast to physiological noise correction however, both MP-PCA and spatial smoothing led to an increase in functional connectivity amplitudes (Table 3 and Figure 4): dorsal-dorsal, ventral-ventral and between-hemicord dorsal-ventral connectivity all had significantly higher amplitudes when compared to the maximal denoising pipeline; the absolute strength of within-hemicord dorsal-ventral connectivity also increased, though with a sign-change, which turned from negative to positive after MP-PCA and smoothing. For all connections, the reliability of functional connectivity increased when spatial smoothing was added to maximal denoising pipeline, whereas a more mixed picture appeared for MP-PCA (with either a slight decrease [dorsal-dorsal and ventral-ventral], increase [between-hemicord] or no change [within-hemicord]; Tables 3 and Figure 4).

One aspect of these results deserves further interrogation, namely whether the increased connectivity amplitudes might simply come about via time-course mixing between the ROIs due to an increased spatial smoothness of the data after the thermal-noise correction procedures. We therefore assessed the spatial autocorrelation function of the EPI data and observed that – across the group – the effective smoothness increased from 1.3±0.66 by 142% for 2mm (3.2±0.15) and 317% for 4mm (5.5±0.28) smoothing. Importantly, despite the more than two-fold increase in tSNR and connectivity amplitudes observed after MP-PCA, this procedure only led to a 34% increase in spatial smoothness (1.8±0.12). It is thus unlikely that the increased connectivity observed after MP-PCA is driven via time-course mixing between the different ROI – an assumption underscored even further by the fact the MP-PCA increased the connectivity of all connections in a way that is unrelated to the ROIs spatial distance (Figure S2). Conversely, the effects of spatial smoothing on connectivity amplitudes are likely driven by time-course mixing, since i) the largest increase e.g. for 2mm smoothing was observed for the ROIs being closest together (dorsal-ventral within-hemicord connection; Figure S2) and ii) the increase in connectivity parallels the increase in spatial smoothness (cf. Figure 4B and 4C). This suggests that even modest smoothing kernels such as 2mm should only be employed with great caution in the spinal cord.

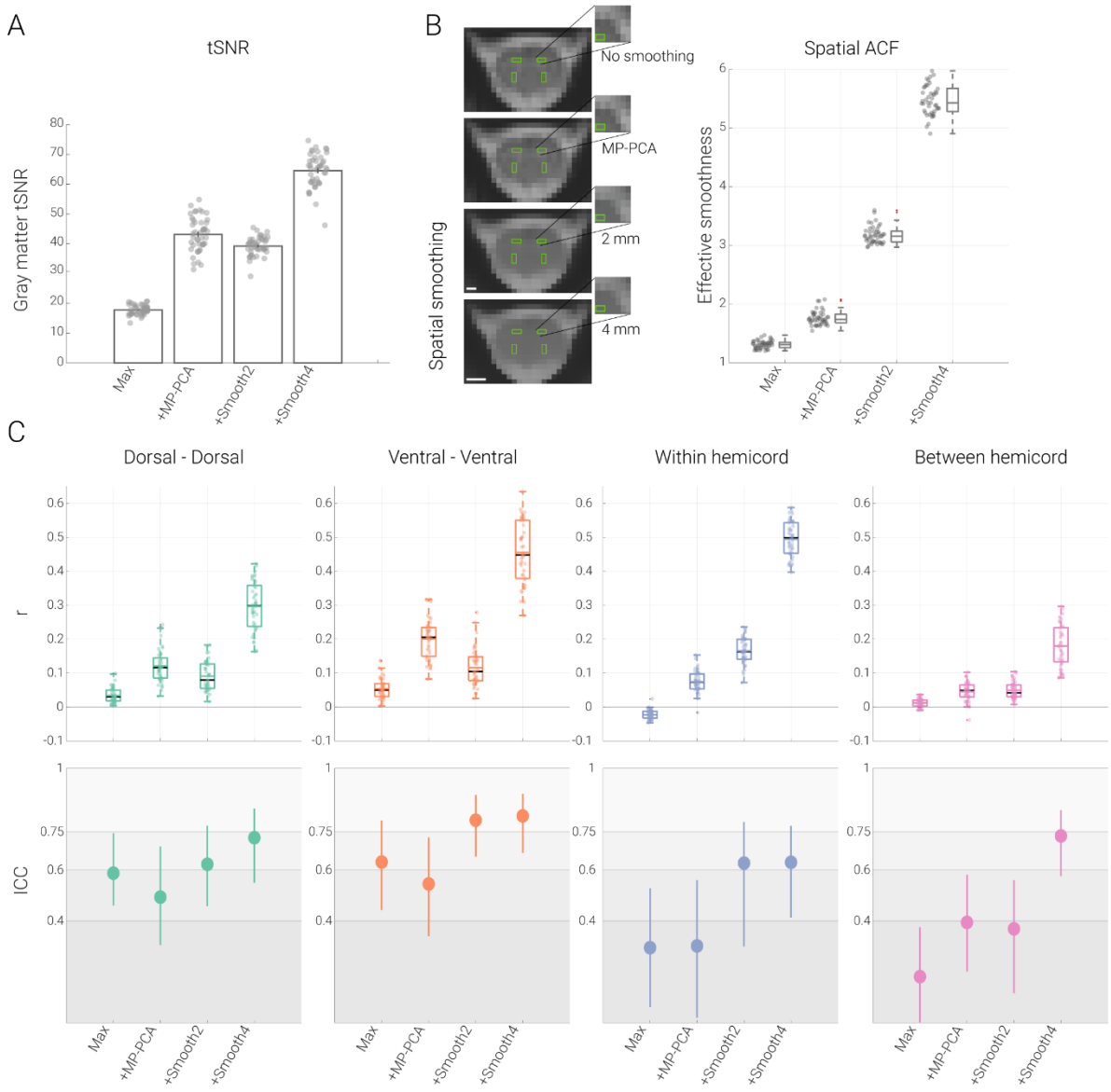

Figure 4. **Impact of thermal noise removal. A. Impact of thermal noise removal on tSNR.** Bar graph shows the tSNR in the gray matter for each segment after employing different processing pipelines (Max: maximal processing – which served as baseline for this comparison, +MP-PCA: maximal + thermal noise removal via MP-PCA; +Smooth2: maximal + smoothing with a 2mm kernel; +Smooth4: maximal + smoothing with a 4mm kernel). The vertical lines on the bars depict the standard error of the mean and the filled dots lines indicate participant-specific values. **B. Impact of thermal noise removal on spatial smoothness.** On the left side, one exemplary EPI slice of a participant in native space (where analyses were carried out) and gray matter ROIs overlaid in green are shown after different processing steps. Scale bars represent 2mm and 4mm, respectively. On the right side, effective spatial smoothness values estimated using AFNI's 3dFWHMx function are depicted via box-plots for which the median is denoted by the central mark and the bottom and top edges of the boxes represent the 25th and 75th percentiles, respectively, with the whiskers encompassing ~99% of the data and outliers being represented by red dots. The circles represent individual participants. **C. Impact of thermal noise removal on functional connectivity and reliability.** The top panel depicts Pearson correlation values (averaged across two sessions) between the time-courses of different ROIs with the box plots for four different pipelines (box plots are identical to those in B – except here the mean is denoted by the colored central mark). On the bottom panel, ICC values for each connection (and each pipeline) are shown with the filled circles and the lines show 95% confidence intervals. The gray scale

622 background reflects the ICC ranges (as defined by Cicchetti & Sparrow (1981) and Hallgren (2012)):
623 poor <0.4, fair 0.4–0.59, good 0.6–0.74, excellent ≥0.75.

624 **3.3. Within-segment functional connectivity**

625 Finally, we aimed to assess whether resting-state functional connectivity could also be reliably
626 observed at the level of single spinal segments (C3, C4, C5, C6, C7, C8 and T1; Figure 5A).
627 For these analyses we used data that were denoised with MP-PCA in addition to the maximal
628 physiological noise correction pipeline, as the above analyses showed this method to be
629 beneficial for both tSNR and connectivity estimates.

630 First of all, we observed that – despite the use of z-shimming – the gray-matter tSNR was lower
631 for the lowermost segments (C7, C8 and T1). Functional connectivity, however, was highly
632 significant in every segment for all connections (dorsal-dorsal, ventral-ventral, within-
633 hemicord, between-hemicord; see Figure 5 and Table 4). Reliability of functional connectivity
634 at the single-segment level, on the other hand, was mostly poor (see Figure 5 and Table 4). For
635 dorsal-dorsal connectivity, the reliability values were largely in the poor range except at level
636 C6 (in the fair range), and for ventral-ventral connectivity, the ICC values fluctuated between
637 the poor and fair range (poor for C3, C6 and C8; fair for C4, C5, C7 and T1). Within- and
638 between-hemicord dorsal-ventral reliability values were in the poor range for every single
639 segment. These results highlight that even though it is possible to detect single-segment
640 connectivity patterns, these are highly variable across scan-sessions and thus lack robustness
641 with the currently employed approaches for data acquisition and analysis.

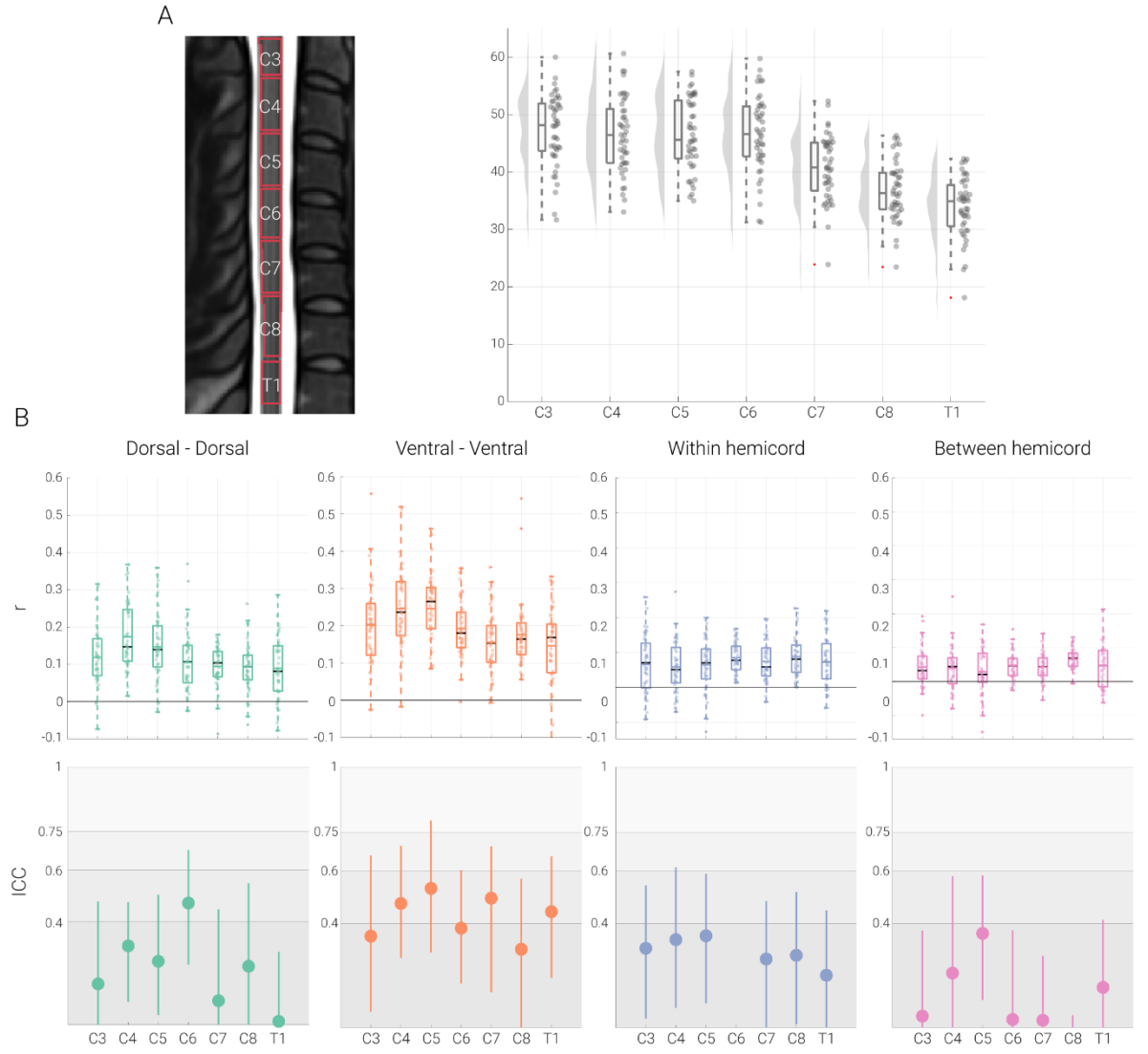

Figure 5. **Segment-specific functional connectivity. A.** The midsagittal cross-section on the left (from the T2-weighted PAM50 template image) shows the thresholded probabilistic segments overlaid as outlines. Segment-wise tSNR values are depicted via box-plots for which the median is denoted by the central mark and the bottom and top edges of the boxes represent the 25th and 75th percentiles, respectively, with the whiskers encompassing ~99% of the data and outliers being represented by red dots. The circles represent individual participants and half-violin plots show the distribution across participants. **B.** The top panel depicts Pearson correlation values (averaged across two sessions) between different ROIs with one box plot per segmental level. For the box plots, the median and mean are denoted by the central black mark and the colored mark, respectively. The bottom and top edges of the boxes represent the 25th and 75th percentiles, respectively, with the whiskers encompassing ~99% of the data, and the outliers are denoted with the red dots. The circles represent individual participants. The bottom panel depicts ICC values for each connection with the dot and the lines denote 95% confidence intervals. The gray scale background reflects the ICC ranges (as defined by Cicchetti & Sparrow (1981) and Hallgren (2012)): poor <0.4, fair 0.4–0.59, good 0.6–0.74, excellent ≥0.75.

4. Discussion

In the last decade, evidence has accumulated that the human spinal cord exhibits spatially distinct patterns of spontaneous activity at rest, as functional connectivity was observed to exist between the two dorsal horns and between the two ventral horns, mirroring the functional division of the gray matter into sensory and motor parts, respectively. While this has generated interest in the use of such connectivity metrics in the clinical context as possible biomarkers for sensory and motor disorders (such as chronic pain and multiple sclerosis), a first essential step is to quantify their reliability, which we set out to do here at the clinically relevant field strength of 3T. We first replicated and extended previous resting-state fMRI findings by investigating the spinal cord's functional connectivity and assessing its test-retest reliability in a large sample (N > 40). Considering that spinal cord BOLD signals are strongly affected by noise, we characterized the impact of various noise sources (i.e., physiological noise and thermal noise) on connectivity strength and reliability. Finally, we considered local aspects of functional connectivity and their reliability by investigating this at a macro-scale unit of spinal cord organization, namely at the level of single spinal segments.

4.1. Replication and extension of previous resting-state functional connectivity results

In order to replicate previously observed functional connectivity results, we used a commonly employed processing pipeline for removal of physiological noise (i.e. addressing noise arising from participant motion, cardiac, respiratory and CSF effects). With an ROI-based approach, we demonstrated statistically significant functional connectivity between the dorsal horns (housing somatosensory function) and between the ventral horns (housing somatomotor function), thus replicating a pattern of results observed in previous spinal cord fMRI studies in rats (Wu et al., 2018), monkeys (Chen et al., 2015; Wu et al., 2019) and humans (3T: Barry et al., 2018; Eippert et al., 2017b; Hu et al., 2018; Liu et al., 2016; Weber et al., 2018 ; 7T: Barry et al., 2014, 2016; Conrad et al., 2018). The fact that such a functional connectivity profile is observed across different acquisition protocols, field strengths as well as species provides further support for the hypothesis that intrinsic fluctuations of the spinal cord are not of random nature. It does however neither confirm the neuronal origin of resting-state functional connectivity nor provide answers regarding the exact neurobiological underpinnings (Eippert & Tracey, 2014) and towards this end, combining fMRI with electrophysiological recordings (Brookes et al., 2011; Schölvinck et al., 2010) would be beneficial, with important first steps in this direction already being taken (Wu et al., 2019).

We also observed significant functional connectivity within (left dorsal-ventral and right dorsal-ventral) and between (left dorsal - right ventral and right dorsal - left ventral) hemicords, though these were clearly weaker in terms of correlation magnitude than the dorsal-dorsal and ventral-ventral connections (and were actually negative for within-hemicord connectivity). This weaker result observed here fits well into the literature, with some studies observing similar sensory-motor cord connectivity (Chen et al., 2015; Weber et al., 2018; Wu et al., 2019), and others not (Barry et al., 2014; Eippert et al., 2017a; see Harrison et al., 2021 for a review). Of note in this case are recent electrophysiological data providing evidence for such

dorsal-ventral connectivity at the level of local field potentials and spike trains in anaesthetized animals (McPherson & Bandres, 2021; Wu et al., 2019). While the reason for this variability of *functional* connectivity findings across experimental models and measurement-levels is currently unclear, existence for *structural* dorsal-ventral connectivity is unequivocal, as it is the anatomical substrate for polysynaptic spinal reflexes in humans (Pierrot-Deseilligny & Burke, 2012; Sandrini et al., 2005) and has also been delineated in detail with modern tracing approaches in mice (e.g. Ronzano et al., 2021; Stepien et al., 2010). Interestingly, in the context of fMRI, the likelihood to observe dorsal-ventral resting-state connectivity might also depend on data processing choices, as this type of result is not robust against variations in the processing pipeline (Eippert et al., 2017a; similar to what we observed here after removal of thermal noise).

One further way to judge the robustness of results is via their reliability, which we assessed here via test-retest reliability (Shrout & Fleiss, 1979). Using ICC as a measure of reliability, we observed fair-to-good reliability for dorsal-dorsal and ventral-ventral connectivity and poor reliability for within hemicord and between hemicord connectivity (the robustness of this finding received further support from analyses in which we employed partial correlation instead of Pearson correlation and observed highly similar results). This is in line with a previous investigation by Barry and colleagues (2016) at the ultra-high field strength of 7T and demonstrates that a similar level of reliability can be obtained at the clinically-relevant field strength of 3T. Previous important investigations into the test-retest reliability of functional connectivity at 3T were limited in terms of the employed sample size (N=10 for Liu et al. (2016), Hu et al. (2018), Barry et al. (2018)), which we overcame here using a more than 4-fold larger sample size. Other studies have assessed the split-half reliability of ICA-derived spinal cord resting-state networks in humans at 3T (Kong et al., 2014) and the test-retest reliability of ROI-based functional connectivity in rats at 9.4T (Wu et al., 2018) and generally observed fair to good reliability as well. It is important to point out that despite these differences in data acquisition and analyses – which have been demonstrated to substantially influence reliability estimates of resting-state connectivity in the brain (for review, see Noble et al. (2019)) – all of these findings seem to point towards reproducible results, i.e. show the presence of reliable spinal cord resting-state networks.

4.2. Impact of noise sources on resting-state functional connectivity and its reliability

Considering that noise has an immense impact on the spinal cord fMRI signal – i.e. its influence is much more prominent than in the brain (Piche et al., 2009; Cohen-Adad et al., 2010) – we next assessed to what degree functional connectivity and its reliability are affected by various noise sources and procedures for their correction.

We first investigated the impact of physiological noise regression on functional connectivity and observed that, in general, extensive denoising (i.e. the addition of various physiological noise regressors to the baseline) led to a clear decrease in the amplitude of functional connectivity estimates and also decreased the reliability of functional connectivity, while – not surprisingly – tSNR was increased. This reduction in amplitude and reliability may seem counterintuitive at first glance, as one might expect that removal of physiological noise should

improve the detectability and reliability of functional connectivity. However, this result is indeed consistent with observations in many resting-state fMRI studies in the brain (Birn et al., 2014; Guo et al., 2012; Noble et al., 2019; Parkes et al., 2018; Shirer et al., 2015; Zou et al., 2015), where a decrease in reliability was observed after various denoising approaches.

Further investigations undertaken to elucidate why reliability decreased after physiological noise removal revealed that the sources of physiological noise – e.g. mean and standard deviation of heart period and breathing period – were highly reliable, i.e. showed stable responses within participants across runs, but large variation across participants (in this sense, we are removing 'true' biological variability here, though of a confounding nature). The same held for the amount gray matter timeseries variance explained by physiological noise regressors: these mostly exhibited reliability in the excellent range, in line with observations in previous studies that also looked at the reproducibility of respiratory and cardiac effects in spinal cord MRI data (Piché et al., 2009; Verma & Cohen-Adad, 2014). If one now considers that our reliability metric of choice – the ICC – can be roughly defined as a ratio of the variance of interest (in our case: between-participant) to the total variance (Liljequist et al., 2019), a possible path via which physiological noise removal decreases reliability becomes apparent: it removes spatiotemporally structured 'reliable artefacts' (i.e. differing strongly between participants, but not necessarily between runs within participants), that would otherwise contribute to the reliability estimation via their confounding effects on connectivity. A similar argument has already been made for the reliability of resting-state connectivity in the brain, substantiated by a detailed investigation of the changes in the different variance components contributing to the ICC (Birn et al., 2014). In other words: once the impact of these *reliable* non-neural sources that influence ROI time-courses similarly – and thus also increase the correlation strength – within each participant is removed, correlation amplitude as well as reliability decreases.

Thus, and as already pointed out by others (Birn et al., 2014; Shirer et al., 2015; Noble et al., 2019), the reduction in reliability after physiological noise removal might actually increase the validity of the results. Validity can be defined as how close or accurate one is measuring what one intends to measure (Carmines & Zeller, 1979) and in our case – using resting-state fMRI – we intend to measure neuronally driven BOLD fluctuations, which only represent a small percentage of the variance in the noisy fMRI signal (Bijsterbosch & Beckmann, 2017; Birn, 2012). One might anticipate that an improved validity after removal of physiological noise may also lead to a better distinction at the group level – e.g. between patients' and healthy controls' functional connectivity patterns – or improve the relationship between functional connectivity estimates and 'trait' characteristics (Shirer et al., 2015; Noble et al., 2017a; Noble et al., 2019); interventional studies could also shed light on this.

In addition to the effects of removing physiological noise, we also assessed the impact of thermal noise (Edelstein et al., 1986; Hoult & Richards, 1976; Krüger & Glover, 2001) and methods for its correction. While we did not formally assess the physiological noise to thermal noise ratio in our data – as this depends on many factors (Brooks et al., 2013; Triantafyllou et al., 2005, 2011) and is complicated by the fact that part of what is traditionally considered physiological 'noise' is our signal of interest here – we observed marked effects of thermal

noise removal: the application of MP-PCA (Veraart et al., 2016a; Veraart et al., 2016b) led to i) a substantial increase in tSNR (more than two-fold), ii) a concurrent and consistent increase in correlation strength (more than three-fold) and iii) no consistent changes in reliability (as we observed either decreases, no change or an increase in reliability, possibly warranting future investigations). One immediately notices the clear difference to physiological noise removal, which also increased the tSNR, but decreased connectivity strength and reliability, likely due to physiological noise being structured and reliable. Despite being a major source of noise in fMRI acquisitions, only a few brain fMRI studies (Ades-Aron et al., 2021a; Adhikari et al., 2019) utilized thermal noise removal via MP-PCA and to our knowledge its benefits for spinal cord fMRI had not yet been demonstrated (see Grussu et al., 2020 for an application of MP-PCA in quantitative MRI of the cord and Vizioli et al., 2021 for an even more recent thermal noise correction technique applied to brain fMRI data). We furthermore compared MP-PCA to spatial smoothing which also serves to suppress thermal noise: compared to spatial smoothing (which also enhanced tSNR and connectivity strength), MP-PCA achieved this without incurring a substantial penalty in terms of increased spatial smoothness. This is an important consideration, since ROIs in the spinal cord lie so close to each other that even with a modest Gaussian smoothing kernel of 2mm FWHM, artificial connectivity (via time-course mixing) can be induced, which we were able to demonstrate here, since the increase in connectivity strength induced via smoothing depended on the spatial proximity of the ROIs. We thus believe that thermal noise removal via MP-PCA might be an attractive option for enhancing the sensitivity of spinal cord fMRI, but would like to note that its detailed validation in the context of resting-state fMRI is still outstanding (as are comparisons with other methods, e.g. Vizioli et al., 2021).

4.3. Within segment functional connectivity

Finally, we assessed the amplitude and reliability of more localized aspects of connectivity, i.e. within a spinal cord segment, which is traditionally considered to be the basic organizational unit of the spinal cord along the rostrocaudal axis (though see Watson & Sidhu, 2009; Sengul et al., 2013). This was made possible by the availability of probabilistic maps for spinal cord segments (Cadotte et al., 2015) and their integration into a common template space (De Leener et al., 2017). Reassuringly, for all of the segmental levels that we investigated (C3-T1), we were able to demonstrate robust functional connectivity patterns, i.e. significantly positive correlations between bilateral dorsal and between bilateral ventral horns, despite an apparent decrease in tSNR for segments C7-T1 compared to the more rostral cervical segments. While minor variations in connectivity strength were observed, the overall pattern stayed consistent across segments and mirrored the above-reported connectivity results that spanned the superior-inferior axis of the imaging volume (similar to Eippert et al. (2017a)). We also observed significant within and between hemicord dorsal-ventral connectivity at each segment (except C5 where between hemicord connectivity was not significant), though this was again much weaker than dorsal-dorsal and ventral-ventral connectivity. Importantly though, the reliability of functional connectivity at the level of individual segments was consistently in the poor range: this held entirely for dorsal-ventral connectivity, mostly for dorsal-dorsal

connectivity (apart from segment C6) and partially for ventral-ventral connectivity (where approximately half of the ICCs were in the fair range); in addition, this was consistently evident across segments and thus not driven by the lower tSNR present in the more caudal segments. Given our 5mm slice thickness, there were only approximately three EPI slices in each segment, probably rendering correlation estimates susceptible to remaining noise across voxels (e.g. compared to the analyses across the imaging volume) and recent investigations have suggested that other 3T acquisition approaches might be helpful in this regard (Kinany et al., 2022), as could be the use of higher field strength (Barry et al., 2018) or using slightly dilated regions of interest. Considering that many disorders present with localized spinal cord pathology (e.g. cervical myelopathy; Nouri et al., 2015) and that spinal cord resting-state fMRI is now being applied in such contexts – e.g. spinal cord injury (Chen et al., 2015; Sengupta et al., 2021) or multiple sclerosis (Conrad et al., 2018; Combes et al., 2022) – it will be of utmost importance to improve the reliability of segment-wise connectivity via optimization of data acquisition and analysis approaches, since only with a reliable estimate of connectivity can longitudinal studies that monitor disease progression or treatment effects be carried out successfully.

4.4. Limitations and outlook

There are several limitations of the current study that are worth mentioning. *First* of all, in terms of assessing functional connectivity, we have only used ROI-based static functional connectivity approaches here, whereas data-driven approaches like ICA (Kong et al., 2014) or time-varying functional connectivity approaches (Kinany et al., 2020) might yield different insights into the reliability of spinal cord networks; of note, these could be applied on our openly-available data-set, allowing for a direct comparison between methods. *Second*, we assessed the impact of physiological noise solely within the PNM framework (Brooks et al., 2008; Kong et al., 2012). Although PNM is well established for spinal cord fMRI and has compared favorably against other methods in this context (Kong et al., 2012), there are many other approaches to address physiological noise that we did not consider here and that again might perform differently, such as CompCor (Behzadi et al., 2007), DRIFTER (Särkkä et al., 2012) or ICA-AROMA (Pruim et al., 2015). A comparison of various denoising approaches was beyond the scope of current work (similar to evaluating the effects of different preprocessing steps), but could also be carried out on this openly-available data-set and might offer additional insights, as there might be unmodeled noise components still present in the data. *Third*, considering the various different approaches for data acquisition that are currently employed in spinal cord fMRI at 3T (e.g. Barry et al., 2021; Kinany et al., 2022), we refrain from extrapolating our results beyond the specific acquisition scheme employed here. *Fourth*, one needs to be careful regarding the interpretation of the observed reliability, since on the one hand, our results may represent an 'upper' end of reliability estimates, as we assessed the test-retest reliability of functional runs which were separated by at most ~10 minutes. On the other hand, the two functional runs had slightly different z-shim settings which might bias towards ‚lower' reliability (although there were no significant tSNR differences between the two acquisitions) . Given these factors, it would be interesting to assess the reliability of resting-

state spinal networks over different time spans in the future, ranging from hours to days to months, as reliability may decrease over time (Shehzad et al., 2009) – here one could also envision to assess runs that were acquired in different scanners (Noble, et al., 2017b) in order probe different components of reliability (Brandmaier et al., 2018). *Finally*, it is important to keep in mind that the ICC is calculated as a ratio of between person variance to total variance and ICC values are thus dependent on the characteristics of given sample. For instance, ICC values for patient groups (such as multiple sclerosis or chronic pain) might be higher due to the larger variability between individual patients as compared to our very homogenous sample consisting of young healthy adults in a very restricted age-range (see also Wenger et al., 2022). Consideration of these aspects might be helpful for understanding the limitations and benefits of spinal cord resting-state fMRI in the clinical context where longitudinal as well as multi-site and multi-cohort studies are common.

5. Conclusion

Taken together, this study adds to a growing body of evidence that the spinal cord exhibits structured resting-state functional connectivity. Connectivity within sensory and within motor regions of the spinal cord seems to be of robust nature, as it presents with fair reliability. Our results furthermore underscore the critical need for addressing physiological noise, though now from the perspective of reliability and also demonstrate that thermal noise removal can have beneficial effects on the detection of functional connectivity. Finally, our assessments of segment-level connectivity (presenting with low reliability) provide a more cautionary note and suggest that further improvements in data acquisition and analysis would be important before employing resting-state spinal cord fMRI longitudinally in the context of assessing disease progression or treatment response.

891 Table 1. *Functional connectivity and reliability after physiological noise correction.*

	Dorsal Dorsal	**Ventral Ventral**	**Within Hemicord**	**Between Hemicord**
Baseline	r = 0.07 t = 12.9 p < 0.001 ICC (95% CI) = 0.71 (0.53 - 0.85)	r = 0.10 t = 18.7 p < 0.001 ICC (95% CI) = 0.65 (0.49 – 0.81)	r = -0.01 t = -4.7 p < 0.001 ICC (95% CI) = 0.38 (0.22 – 0.54)	r = 0.02 t = 7.1 p < 0.001 ICC (95% CI) = 0.28 (0.11 – 0.47)
Baseline + Motion parameters	r = 0.06 t = 12.4 p < 0.001 ICC (95% CI) = 0.68 (0.52 0.82)	r = 0.09 t = 17.4 p < 0.001 ICC (95% CI) = 0.69 (0.54 – 0.84)	r = -0.02 t = -4.7 p < 0.001 ICC (95% CI) = 0.36 (0.19 – 0.51)	r = 0.01 t = 7.7 p < 0.001 ICC (95% CI) = 0.23 (0.02 – 0.44)
Baseline + CSF	r = 0.06 t = 12.9 p < 0.001 ICC (95% CI) = 0.69 (0.52 – 0.84)	r = 0.09 t = 16.9 p < 0.001 ICC (95% CI) = 0.67 (0.46 – 0.82)	r = -0.01 t = -7.7 p < 0.001 ICC (95% CI) = 0.39 (0.23 – 0.54)	r = 0.02 t = 6.0 p < 0.001 ICC (95% CI) = 0.32 (0.16 – 0.48)
Baseline + Respiratory	r = 0.06 t = 12.8 p < 0.001 ICC (95% CI) = 0.65 (0.44 – 0.81)	r = 0.09 t = 16.6 p < 0.001 ICC (95% CI) = 0.68 (0.52 – 0.83)	r = -0.02 t = -8.1 p < 0.001 ICC (95% CI) = 0.37 (0.18 – 0.54)	r = 0.01 t = 5.7 p < 0.001 ICC (95% CI) = 0.29 (0.09 – 0.47)
Baseline + Cardiac	r = 0.05 t = 10.8 p < 0.001 ICC (95% CI) = 0.66 (0.45 – 0.84)	r = 0.08 t = 15.0 p < 0.001 ICC (95% CI) = 0.63 (0.44 – 0.78)	r = -0.01 t = -5.5 p < 0.001 ICC (95% CI) = 0.35 (0.12 – 0.55)	r = 0.02 t = 8.4 p < 0.001 ICC (95% CI) = 0.29 (0.10 – 0.47)
Baseline + PNM	r = 0.04 t = 9.8 p < 0.001 ICC (95% CI) = 0.64 (0.48 – 0.79)	r = 0.06 t = 12.4 p < 0.001 ICC (95% CI) = 0.62 (0.41 – 0. 79)	r = -0.02 t = -9.4 p < 0.001 ICC (95% CI) = 0.31 (0.06 – 0.56)	r = 0.01 t = 6.7 p < 0.001 ICC (95% CI) = 0.25 (0.02 – 0.44)
Maximal	r = 0.03 t = 9.5 p < 0.001 ICC (95% CI) = 0.59 (0.46 – 0.74)	r = 0.05 t = 11.6 p < 0.001 ICC (95% CI) = 0.63 (0.44 – 0.79)	r = -0.02 t = -10.7 p < 0.001 ICC (95% CI) = 0.30 (0.06 – 0.53)	r = 0.01 t = 6.7 p < 0.001 ICC (95% CI) = 0.18 (-0.03 – 0.38)

892 This table depicts functional connectivity and reliability results of each connection across seven denoising pipelines. r represents the
893 mean Pearson correlation across participants, and t and p represent the t-value and two-tailed FWE-corrected (for seven tests) p-value
894 from a permutation test (against 0), respectively. ICC(95% CI) represents ICC(2,1) values and 95% bootstrapped confidence intervals.

895

Table 2. *Comparison of functional connectivity strength for different denoising pipelines.*

	Dorsal Dorsal	**Ventral Ventral**	**Within Hemicord**	**Between Hemicord**
Baseline + Motion parameters	t(44) = -8.0 p < 0.001	t(44) = -9.9 p < 0.001	t(44) = -6.1 p < 0.001	t(44) = -5.1 p < 0.001
Baseline + CSF	t(44) = -6.6 p < 0.001	t(44) = -8.1 p < 0.001	t(44) = 0.4 p = 0.98	t(44) = -0.6 p = 0.93
Baseline + Respiratory	t(44) = -8.8 p < 0.001	t(44) = -11.3 p < 0.001	t(44) = -7.0 p < 0.001	t(44) = -6.1 p < 0.001
Baseline + Cardiac	t(44) = -10.5 p < 0.001	t(44) = -11.1 p < 0.001	t(44) = -1.0 p = 0.68	t(44) = 1.1 p = 0.64
Baseline + PNM	t(44) = -11.4 p < 0.001	t(44) = -16.3 p < 0.001	t(44) = -5.6 p < 0.001	t(44) = -2.6 p = 0.04
Maximal	t(44) = -11.6 p < 0.001	t(44) = -17.8 p < 0.001	t(44) = -5.9 p < 0.001	t(44) = -3.0 p = 0.01

This table depicts statistical comparisons of the functional connectivity strength (for each of the four connections) for six different denoising pipelines against the baseline pipeline. t and p represent the t-value and two-tailed FWE-corrected (for six tests) p-value from a permutation test against 0 (as values for each connection were subtracted from the baseline functional connectivity values). Note that for within hemicord connectivity (where connectivity values are negative), smaller t-values mean that the negative connectivity gets stronger.

903 Table 3. *Functional connectivity and its reliability after thermal noise correction procedures.*

	Dorsal Dorsal	**Ventral Ventral**	**Within Hemicord**	**Between Hemicord**
Maximal	r = 0.03 t = 9.5 p < 0.001 ICC (95% CI) = 0.59 (0.46 – 0.74)	r = 0.05 t = 11.6 p < 0.001 ICC (95% CI) = 0.63 (0.44 – 0.79)	r = -0.02 t = -10.7 p < 0.001 ICC (95% CI) = 0.30 (0.06 – 0.53)	r = 0.01 t = 6.7 p < 0.001 ICC (95% CI) = 0.18 (-0.03 – 0.38)
Thermal noise removal + maximal	r = 0.12 t = 16.7 p < 0.001 ICC (95% CI) = 0.49 (0.31 – 0.69)	r = 0.20 t = 22.9 p < 0.001 ICC (95% CI) = 0.55 (0.34 – 0.73)	r = 0.07 t = 15.6 p < 0.001 ICC (95% CI) = 0.30 (0.02 – 0.56)	r = 0.05 t = 10.6 p < 0.001 ICC (95% CI) = 0.39 (0.20 – 0.58)
Maximal + 2mm smoothing	r = 0.09 t = 14.3 p < 0.001 ICC (95% CI) = 0.62 (0.46 – 0.77)	r = 0.12 t = 13.9 p < 0.001 ICC (95% CI) = 0.79 (0.65 – 0.89)	r = 0.17 t = 29.1 p < 0.001 ICC (95% CI) = 0.63 (0.30 – 0.79)	r = 0.05 t = 13.4 p < 0.001 ICC (95% CI) = 0.37 (0.12 – 0.56)
Maximal + 4mm smoothing	r = 0.29 t = 28.3 p < 0.001 ICC (95% CI) = 0.73 (0.55 – 0.84)	r = 0.46 t = 33.6 p < 0.001 ICC (95% CI) = 0.81 (0.67 – 0.89)	r = 0.49 t = 64.4 p < 0.001 ICC (95% CI) = 0.63 (0.41 – 0.77)	r = 0.18 t = 19.8 p < 0.001 ICC (95% CI) = 0.73 (0.58 – 0.84)

904 This table depicts functional connectivity and reliability results of each connection for different thermal noise correction processing
905 pipelines. r represents the mean Pearson correlation across participants, t and p represent the t-value and two-tailed FWE-corrected
906 (for four tests) p-value from a permutation test (against 0), respectively. ICC(95% CI) represents ICC(2,1) values and 95%
907 bootstrapped confidence intervals.

908

909 Table 4. *Functional connectivity and its reliability for different spinal segments.*

	Dorsal Dorsal	**Ventral Ventral**	**Within Hemicord**	**Between Hemicord**
C3	r = 0.12 t = 9.2 p < 0.001 ICC (95% CI) = 0.16 (-0.24 – 0.48)	r = 0.20 t = 8.9 p < 0.001 ICC (95% CI) = 0.35 (0.06 – 0.66)	r = 0.07 t = 5.0 p < 0.001 ICC (95% CI) = 0.30 (0.03 – 0.55)	r = 0.04 t = 4.6 p < 0.001 ICC (95% CI) = 0.04 (-0.23 – 0.37)
C4	r = 0.17 t = 13.6 p < 0.001 ICC (95% CI) = 0.31 (0.09 – 0.48)	r = 0.25 t = 13.3 p < 0.001 ICC (95% CI) = 0.48 (0.27 – 0.69)	r = 0.06 t = 5.5 p < 0.001 ICC (95% CI) = 0.34 (0.08 – 0.61)	r = 0.04 t = 4.2 p < 0.001 ICC (95% CI) = 0.21 (-0.07 – 0.58)
C5	r = 0.15 t = 10.9 p < 0.001 ICC (95% CI) = 0.25 (0.04 – 0.50)	r = 0.25 t = 12.5 p < 0.001 ICC (95% CI) = 0.53 (0.29 – 0.79)	r = 0.06 t = 5.7 p < 0.001 ICC (95% CI) = 0.35 (0.09 – 0.59)	r = 0.03 t = 2.6 p = 0.07 ICC (95% CI) = 0.36 (0.11 – 0.58)
C6	r = 0.11 t = 7.5 p < 0.001 ICC (95% CI) = 0.47 (0.23 – 0.68)	r = 0.19 t = 16.3 p < 0.001 ICC (95% CI) = 0.38 (0.17 – 0.60)	r = 0.09 t = 12.4 p < 0.001 ICC (95% CI) = -0.24 (-0.52 – 0.0)	r = 0.05 t = 7.5 p < 0.001 ICC (95% CI) = 0.03 (-0.45 – 0.37)
C7	r = 0.09 t = 11.5 p < 0.001 ICC (95% CI) = 0.09 (-0.29 – 0.45)	r = 0.16 t = 18.2 p < 0.001 ICC (95% CI) = 0.49 (0.14 – 0.69)	r = 0.07 t = 8.1 p < 0.001 ICC (95% CI) = 0.26 (0.0 – 0.49)	r = 0.04 t = 7.2 p < 0.001 ICC (95% CI) = 0.03 (-0.23 – 0.28)
C8	r = 0.049 t = 9.5 p < 0.001 ICC (95% CI) = 0.23 (-0.20 – 0.55)	r = 0.18 t = 16.6 p < 0.001 ICC (95% CI) = 0.30 (-0.13 – 0.57)	r = 0.09 t = 9.9 p < 0.001 ICC (95% CI) = 0.28 (0.01 – 0.52)	r = 0.07 t = 14.0 p < 0.001 ICC (95% CI) = -0.23 (-0.46 – 0.04)
T1	r = 0.09 t = 7.0 p < 0.001 ICC (95% CI) = 0.01 (-0.22 – 0.28)	r = 0.15 t = 12.2 p < 0.001 ICC (95% CI) = 0.44 (0.19 – 0.66)	r = 0.07 t = 6.9 p < 0.001 ICC (95% CI) = 0.20 (-0.09 – 0.45)	r = 0.05 t = 4.8 p < 0.001 ICC (95% CI) = 0.15 (-0.09 – 0.41)

910 This table depicts functional connectivity and reliability results of each connection at different spinal segments. r represents the mean
911 Pearson correlation across participants, t and p represent the t-value and two-tailed family-wise-error corrected p-value from a
912 permutation test (against 0), respectively. ICC (95% CI) represents ICC(2,1) values and 95% bootstrapped confidence intervals.

References

Ades-Aron, B., Lemberskiy, G., Veraart, J., Golfinos, J., Fieremans, E., Novikov, D. S., & Shepherd, T. (2021a). Improved Task-based Functional MRI Language Mapping in Patients with Brain Tumors through Marchenko-Pastur Principal Component Analysis Denoising. *Radiology*, *298*(2), 365–373. https://doi.org/10.1148/radiol.2020200822

Ades-Aron, B., Coelho, S., Veraart, J., Lemberskiy, G., Barroll, G., Baete, S., Shepherd, T., Novikov, D.S. and Fieremans, E., Random matrix theory denoising minimizes cross-scanner,-protocol variability and maximizes repeatability of higher-order diffusion metrics. ISMRM Annual Meeting, Online 15-20 May 2021b.

Adhikari, B. M., Jahanshad, N., Shukla, D., Turner, J., Grotegerd, D., Dannlowski, U., Kugel, H., Engelen, J., Dietsche, B., Krug, A., Kircher, T., Fieremans, E., Veraart, J., Novikov, D. S., Boedhoe, P. S. W., van der Werf, Y. D., van den Heuvel, O. A., Ipser, J., Uhlmann, A., … Kochunov, P. (2019). A resting state fMRI analysis pipeline for pooling inference across diverse cohorts: An ENIGMA rs-fMRI protocol. *Brain Imaging and Behavior*, *13*(5), 1453–1467. https://doi.org/10.1007/s11682-018-9941-x

Bach, D. R., Gerster, S., Tzovara, A., & Castegnetti, G. (2016). A linear model for event-related respiration responses. *Journal of Neuroscience Methods*, *270*, 147–155. https://doi.org/10.1016/j.jneumeth.2016.06.001

Barry, R. L., Conrad, B. N., Smith, S. A., & Gore, J. C. (2018). A practical protocol for measurements of spinal cord functional connectivity. *Scientific Reports*, *8*(1), 16512. https://doi.org/10.1038/s41598-018-34841-6

Barry, R. L., Rogers, B. P., Conrad, B. N., Smith, S. A., & Gore, J. C. (2016). Reproducibility of resting state spinal cord networks in healthy volunteers at 7 Tesla. *NeuroImage*, *133*, 31–40. https://doi.org/10.1016/j.neuroimage.2016.02.058

Barry, R. L., Smith, S. A., Dula, A. N., & Gore, J. C. (2014). Resting state functional connectivity in the human spinal cord. *ELife*, *3*, e02812. https://doi.org/10.7554/eLife.02812

Behzadi, Y., Restom, K., Liau, J., & Liu, T. T. (2007). A Component Based Noise Correction Method (CompCor) for BOLD and Perfusion Based fMRI. *NeuroImage*, *37*(1), 90–101. https://doi.org/10.1016/j.neuroimage.2007.04.042

Bijsterbosch, J., & Beckmann, C. (2017). *An Introduction to Resting State FMRI Functional Connectivity*. Oxford University Press.

Birn, R. M. (2012). The role of physiological noise in resting-state functional connectivity. *NeuroImage*, *62*(2), 864–870. https://doi.org/10.1016/j.neuroimage.2012.01.016

Birn, R. M., Cornejo, M. D., Molloy, E. K., Patriat, R., Meier, T. B., Kirk, G. R., Nair, V. A., Meyerand, M. E., & Prabhakaran, V. (2014). The influence of physiological noise correction on test-retest reliability of resting-state functional connectivity. *Brain Connectivity*, *4*(7), 511–522. https://doi.org/10.1089/brain.2014.0284

Brandmaier, A. M., Wenger, E., Bodammer, N. C., Kühn, S., Raz, N., & Lindenberger, U. (2018). Assessing reliability in neuroimaging research through intra-class effect decomposition (ICED). *ELife*, *7*, e35718. https://doi.org/10.7554/eLife.35718

Brookes, M. J., Woolrich, M., Luckhoo, H., Price, D., Hale, J. R., Stephenson, M. C., Barnes, G. R., Smith, S. M., & Morris, P. G. (2011). Investigating the electrophysiological basis of resting state networks using magnetoencephalography. *Proceedings of the National Academy of Sciences*, *108*(40), 16783–16788. https://doi.org/10.1073/pnas.1112685108

Brooks, J. C. W., Beckmann, C. F., Miller, K. L., Wise, R. G., Porro, C. A., Tracey, I., & Jenkinson, M. (2008). Physiological noise modelling for spinal functional magnetic resonance imaging studies. *NeuroImage*, *39*(2), 680–692. https://doi.org/10.1016/j.neuroimage.2007.09.018

Brooks, J., Faull, O., Pattinson, K., & Jenkinson, M. (2013). Physiological Noise in Brainstem fMRI. *Frontiers in Human Neuroscience*, *7*. https://www.frontiersin.org/article/10.3389/fnhum.2013.00623

Cadotte, D. W., Cadotte, A., Cohen-Adad, J., Fleet, D., Livne, M., Wilson, J. R., Mikulis, D., Nugaeva, N., & Fehlings, M. G. (2015). Characterizing the Location of Spinal and Vertebral Levels in the Human Cervical Spinal Cord. *American Journal of Neuroradiology*, *36*(4), 803–810. https://doi.org/10.3174/ajnr.A4192

Chen, L. M., Mishra, A., Yang, P.-F., Wang, F., & Gore, J. C. (2015). Injury alters intrinsic functional connectivity within the primate spinal cord. *Proceedings of the National Academy of Sciences*, *112*(19), 5991–5996. https://doi.org/10.1073/pnas.1424106112

Cicchetti, D. V., & Sparrow, S. A. (1981). Developing criteria for establishing interrater reliability of specific items: Applications to assessment of adaptive behavior. *American Journal of Mental Deficiency*, *86*(2), 127–137.

Cohen-Adad, J., Alonso-Ortiz, E., Abramovic, M., Arneitz, C., Atcheson, N., Barlow, L., Barry, R. L., Barth, M., Battiston, M., Büchel, C., Budde, M., Callot, V., Combes, A. J. E., De Leener, B., Descoteaux, M., de Sousa, P. L., Dostál, M., Doyon, J., Dvorak, A., … Xu, J. (2021). Generic acquisition protocol for quantitative MRI of the spinal cord. *Nature Protocols*, *16*(10), 4611–4632. https://doi.org/10.1038/s41596-021-00588-0

Combes, A. J. E., O'Grady, K. P., Rogers, B. P., Schilling, K. G., Lawless, R. D., Visagie, M., Houston, D., Prock, L., Malone, S., Satish, S., Witt, A. A., McKnight, C. D., Bagnato, F., Gore, J. C., & Smith, S. A. (2022). Functional connectivity in the dorsal network of the cervical spinal cord is correlated with diffusion tensor imaging indices in relapsing-remitting multiple sclerosis. *NeuroImage : Clinical*, *35*, 103127. https://doi.org/10.1016/j.nicl.2022.103127

Conrad, B. N., Barry, R. L., Rogers, B. P., Maki, S., Mishra, A., Thukral, S., Sriram, S., Bhatia, A., Pawate, S., Gore, J. C., & Smith, S. A. (2018). Multiple sclerosis lesions affect intrinsic functional connectivity of the spinal cord. *Brain*, *141*(6), 1650–1664. https://doi.org/10.1093/brain/awy083

Corey, D. M., Dunlap, W. P., & Burke, M. J. (1998). Averaging Correlations: Expected Values and Bias in Combined Pearson rs and Fisher's z Transformations. *The Journal of General Psychology*, *125*(3), 245–261. https://doi.org/10.1080/00221309809595548

Cox, R. W., Chen, G., Glen, D. R., Reynolds, R. C., & Taylor, P. A. (2017). FMRI Clustering in AFNI: False-Positive Rates Redux. *Brain Connectivity*, *7*(3), 152–171. https://doi.org/10.1089/brain.2016.0475

De Leener, B., Fonov, V. S., Collins, D. L., Callot, V., Stikov, N., & Cohen-Adad, J. (2018). PAM50: Unbiased multimodal template of the brainstem and spinal cord aligned with the ICBM152 space. *NeuroImage*, *165*, 170–179. https://doi.org/10.1016/j.neuroimage.2017.10.041

De Leener, B., Lévy, S., Dupont, S. M., Fonov, V. S., Stikov, N., Louis Collins, D., Callot, V., & Cohen-Adad, J. (2017). SCT: Spinal Cord Toolbox, an open-source software for processing spinal cord MRI data. *NeuroImage*, *145*, 24–43. https://doi.org/10.1016/j.neuroimage.2016.10.009

Deco, G., Jirsa, V. K., & McIntosh, A. R. (2011). Emerging concepts for the dynamical organization of resting-state activity in the brain. *Nature Reviews. Neuroscience*, *12*(1), 43–56. https://doi.org/10.1038/nrn2961

Delorme, A., & Makeig, S. (2004). EEGLAB: An open source toolbox for analysis of single-trial EEG dynamics including independent component analysis. *Journal of Neuroscience Methods*, *134*(1), 9–21. https://doi.org/10.1016/j.jneumeth.2003.10.009

Edelstein, W. A., Glover, G. H., Hardy, C. J., & Redington, R. W. (1986). The intrinsic signal-to-noise ratio in NMR imaging. *Magnetic Resonance in Medicine*, *3*(4), 604–618. https://doi.org/10.1002/mrm.1910030413

Eippert, F., Kong, Y., Winkler, A. M., Andersson, J. L., Finsterbusch, J., Büchel, C., Brooks, J. C. W., & Tracey, I. (2017a). Investigating resting-state functional connectivity in the cervical spinal cord at 3 T. *NeuroImage*, *147*, 589–601. https://doi.org/10.1016/j.neuroimage.2016.12.072

Eippert, F., Kong, Y., Winkler, A. M., Andersson, J. L., Finsterbusch, J., Büchel, C., Brooks, J. C. W., & Tracey, I. (2017b). Investigating resting-state functional connectivity in the cervical spinal cord at 3 T. *Neuroimage*, *147*, 589–601. https://doi.org/10.1016/j.neuroimage.2016.12.072

Eippert, F., & Tracey, I. (2014). The spinal cord is never at rest. *ELife*, *3*, e03811. https://doi.org/10.7554/eLife.03811

Finsterbusch, J., Eippert, F., & Büchel, C. (2012). Single, slice-specific z-shim gradient pulses improve T2*-weighted imaging of the spinal cord. *NeuroImage*, *59*(3), 2307–2315. https://doi.org/10.1016/j.neuroimage.2011.09.038

Fox, M. D., & Raichle, M. E. (2007). Spontaneous fluctuations in brain activity observed with functional magnetic resonance imaging. *Nature Reviews Neuroscience*, *8*(9), 700–711. https://doi.org/10.1038/nrn2201

Glover, G. H., Li, T.-Q., & Ress, D. (2000). Image-based method for retrospective correction of physiological motion effects in fMRI: RETROICOR. *Magnetic Resonance in Medicine*, *44*(1), 162–167. https://doi.org/10.1002/1522-2594(200007)44:1<162::AID-MRM23>3.0.CO;2-E

Gros, C., De Leener, B., Badji, A., Maranzano, J., Eden, D., Dupont, S. M., Talbott, J., Zhuoquiong, R., Liu, Y., Granberg, T., Ouellette, R., Tachibana, Y., Hori, M., Kamiya, K., Chougar, L., Stawiarz, L., Hillert, J., Bannier, E., Kerbrat, A., … Cohen-Adad, J. (2019). Automatic segmentation of the spinal cord and intramedullary multiple sclerosis lesions with convolutional neural networks. *NeuroImage*, *184*, 901–915. https://doi.org/10.1016/j.neuroimage.2018.09.081

Grussu, F., Battiston, M., Veraart, J., Schneider, T., Cohen-Adad, J., Shepherd, T. M., Alexander, D. C., Fieremans, E., Novikov, D. S., & Gandini Wheeler-Kingshott, C. A. M. (2020). Multi-parametric quantitative in vivo spinal cord MRI with unified signal readout and image denoising. *NeuroImage*, *217*, 116884. https://doi.org/10.1016/j.neuroimage.2020.116884

Guo, C. C., Kurth, F., Zhou, J., Mayer, E. A., Eickhoff, S. B., Kramer, J. H., & Seeley, W. W. (2012). One-year test–retest reliability of intrinsic connectivity network fMRI in older adults. *NeuroImage*, *61*(4), 1471–1483. https://doi.org/10.1016/j.neuroimage.2012.03.027

Hallgren, K. A. (2012). Computing Inter-Rater Reliability for Observational Data: An Overview and Tutorial. *Tutorials in Quantitative Methods for Psychology*, *8*(1), 23–34.

Hallquist, M. N., Hwang, K., & Luna, B. (2013). The Nuisance of Nuisance Regression: Spectral Misspecification in a Common Approach to Resting-State fMRI Preprocessing Reintroduces Noise and Obscures Functional Connectivity. *NeuroImage*, *0*, 208–225. https://doi.org/10.1016/j.neuroimage.2013.05.116

Harita, S., Ioachim, G., Powers, J., & Stroman, P. W. (2019). Investigation of Resting-State BOLD Networks in the Human Brainstem and Spinal Cord. *Neuroscience*, *404*, 71–81. https://doi.org/10.1016/j.neuroscience.2019.02.009

Harita, S., & Stroman, P. W. (2017). Confirmation of resting-state BOLD fluctuations in the human brainstem and spinal cord after identification and removal of physiological noise. *Magnetic Resonance in Medicine*, *78*(6), 2149–2156. https://doi.org/10.1002/mrm.26606

Harrison, O. K., Guell, X., Klein-Flügge, M. C., & Barry, R. L. (2021). Structural and resting state functional connectivity beyond the cortex. *NeuroImage*, *240*, 118379. https://doi.org/10.1016/j.neuroimage.2021.118379

Hochman, S. (2007). Spinal cord. *Current Biology*, *17*(22), R950–R955. https://doi.org/10.1016/j.cub.2007.10.014

Hohenfeld, C., Werner, C. J., & Reetz, K. (2018). Resting-state connectivity in neurodegenerative disorders: Is there potential for an imaging biomarker? *NeuroImage: Clinical*, *18*, 849–870. https://doi.org/10.1016/j.nicl.2018.03.013

Hoult, D. I., & Richards, R. E. (1976). The signal-to-noise ratio of the nuclear magnetic resonance experiment. *Journal of Magnetic Resonance (1969)*, *24*(1), 71–85. https://doi.org/10.1016/0022-2364(76)90233-X

Hu, Y., Jin, R., Li, G., Luk, K. D., & Wu, Ed. X. (2018). Robust spinal cord resting-state fMRI using independent component analysis-based nuisance regression noise reduction: Robust Spinal Cord rsfMRI Using ICANR. *Journal of Magnetic Resonance Imaging*, *48*(5), 1421–1431. https://doi.org/10.1002/jmri.26048

Ioachim, G., Powers, J. M., & Stroman, P. W. (2019). Comparing Coordinated Networks Across the Brainstem and Spinal Cord in the Resting State and Altered Cognitive State. Brain Connectivity, 9(5), 415–424. https://doi.org/10.1089/brain.2018.0659

Ioachim, G., Powers, J. M., Warren, H. J. M., & Stroman, P. W. (2020). Coordinated Human Brainstem and Spinal Cord Networks during the Expectation of Pain Have Elements Unique from Resting-State Effects. Brain Sciences, 10(9), 568. https://doi.org/10.3390/brainsci10090568

Jenkinson, M., Beckmann, C. F., Behrens, T. E. J., Woolrich, M. W., & Smith, S. M. (2012). FSL. *NeuroImage*, *62*(2), 782–790. https://doi.org/10.1016/j.neuroimage.2011.09.015

Kaptan, M., Vannesjo, S. J., Mildner, T., Horn, U., Hartley-Davies, R., Oliva, V., Brooks, J. C. W., Weiskopf, N., Finsterbusch, J., & Eippert, F. (n.d.). Automated slice-specific z-shimming for functional magnetic resonance imaging of the human spinal cord. *Human Brain Mapping*, *n/a*(n/a). https://doi.org/10.1002/hbm.26018

Kinany, N., Pirondini, E., Mattera, L., Martuzzi, R., Micera, S., & Van De Ville, D. (2022). Towards reliable spinal cord fMRI: Assessment of common imaging protocols. *NeuroImage*, *250*, 118964. https://doi.org/10.1016/j.neuroimage.2022.118964

Kinany, N., Pirondini, E., Micera, S., & Van De Ville, D. (2020). Dynamic Functional Connectivity of Resting-State Spinal Cord fMRI Reveals Fine-Grained Intrinsic Architecture. *Neuron*, *108*(3), 424-435.e4. https://doi.org/10.1016/j.neuron.2020.07.024

Ko, H.-Y., Park, J. H., Shin, Y. B., & Baek, S. Y. (2004). Gross quantitative measurements of spinal cord segments in human. *Spinal Cord*, *42*(1), 35–40. https://doi.org/10.1038/sj.sc.3101538

Kong, Y., Eippert, F., Beckmann, C. F., Andersson, J., Finsterbusch, J., Büchel, C., Tracey, I., & Brooks, J. C. W. (2014). Intrinsically organized resting state networks in the human spinal cord. *Proceedings of the National Academy of Sciences*, *111*(50), 18067–18072. https://doi.org/10.1073/pnas.1414293111

Kong, Y., Jenkinson, M., Andersson, J., Tracey, I., & Brooks, J. C. W. (2012). Assessment of physiological noise modelling methods for functional imaging of the spinal cord. *NeuroImage*, *60*(2), 1538–1549. https://doi.org/10.1016/j.neuroimage.2011.11.077

Krüger, G., & Glover, G. H. (2001). Physiological noise in oxygenation-sensitive magnetic resonance imaging. *Magnetic Resonance in Medicine*, *46*(4), 631–637. https://doi.org/10.1002/mrm.1240

Liljequist, D., Elfving, B., & Roaldsen, K. S. (2019). Intraclass correlation – A discussion and demonstration of basic features. *PLOS ONE*, *14*(7), e0219854. https://doi.org/10.1371/journal.pone.0219854

Liu, X., Zhou, F., Li, X., Qian, W., Cui, J., Zhou, I. Y., Luk, K. D. K., Wu, Ed. X., & Hu, Y. (2016a). Organization of the intrinsic functional network in the cervical spinal cord: A resting state functional MRI study. *Neuroscience*, *336*, 30–38. https://doi.org/10.1016/j.neuroscience.2016.08.042

Liu, X., Qian, W., Jin, R., Li, X., Luk, K. D., Wu, E. X., & Hu, Y. (2016). Amplitude of Low Frequency Fluctuation (ALFF) in the Cervical Spinal Cord with Stenosis: A Resting State fMRI Study. *PloS One, 11*(12), e0167279. https://doi.org/10.1371/journal.pone.0167279

Marčenko, V. A., & Pastur, L. A. (1967). DISTRIBUTION OF EIGENVALUES FOR SOME SETS OF RANDOM MATRICES. *Mathematics of the USSR-Sbornik*, *1*(4), 457–483. https://doi.org/10.1070/SM1967v001n04ABEH001994

Martucci, K. T., Weber, K. A., & Mackey, S. C. (2021). Spinal Cord Resting State Activity in Individuals With Fibromyalgia Who Take Opioids. *Frontiers in Neurology, 12*. https://www.frontiersin.org/articles/10.3389/fneur.2021.694271

Martucci, K. T., Weber II, K. A., & Mackey, S. C. (2019). Altered Cervical Spinal Cord Resting-State Activity in Fibromyalgia. *Arthritis & Rheumatology*, *71*(3), 441–450. https://doi.org/10.1002/art.40746

McGraw, K. O., & Wong, S. P. (1996). Forming inferences about some intraclass correlation coefficients. *Psychological Methods*, *1*, 30–46. https://doi.org/10.1037/1082-989X.1.1.30

McPherson, J. G., & Bandres, M. F. (2021). Spontaneous neural synchrony links intrinsic spinal sensory and motor networks during unconsciousness. *ELife*, *10*, e66308. https://doi.org/10.7554/eLife.66308

Molloy, E.K. and Birn, R.M. (2014). Tools for test-retest FMRI studies. ZENODO. DOI:10.5281/zenodo.49326.

Murphy, K., Birn, R. M., & Bandettini, P. A. (2013). Resting-state fMRI confounds and cleanup. *NeuroImage*, *80*, 349–359. https://doi.org/10.1016/j.neuroimage.2013.04.001

Niazy, R. K., Beckmann, C. F., Iannetti, G. D., Brady, J. M., & Smith, S. M. (2005). Removal of FMRI environment artifacts from EEG data using optimal basis sets. *NeuroImage*, *28*(3), 720–737. https://doi.org/10.1016/j.neuroimage.2005.06.067

Noble, S., Scheinost, D., & Constable, R. T. (2019). A decade of test-retest reliability of functional connectivity: A systematic review and meta-analysis. *NeuroImage*, *203*, 116157. https://doi.org/10.1016/j.neuroimage.2019.116157

Noble, S., Spann, M. N., Tokoglu, F., Shen, X., Constable, R. T., & Scheinost, D. (2017a). Influences on the Test–Retest Reliability of Functional Connectivity MRI and its Relationship with Behavioral Utility. *Cerebral Cortex*, *27*(11), 5415–5429.

Noble, S., Scheinost, D., Finn, E. S., Shen, X., Papademetris, X., McEwen, S. C., Bearden, C. E., Addington, J., Goodyear, B., Cadenhead, K. S., Mirzakhanian, H., Cornblatt, B. A., Olvet, D. M., Mathalon, D. H., McGlashan, T. H., Perkins, D. O., Belger, A., Seidman, L. J., Thermenos, H., … Constable, R. T. (2017). Multisite reliability of MR-based functional connectivity. *NeuroImage*, *146*, 959–970. https://doi.org/10.1016/j.neuroimage.2016.10.020

Parkes, L., Fulcher, B., Yücel, M., & Fornito, A. (2018). An evaluation of the efficacy, reliability, and sensitivity of motion correction strategies for resting-state functional MRI. *NeuroImage*, *171*, 415–436. https://doi.org/10.1016/j.neuroimage.2017.12.073

Parrish, T. B., Gitelman, D. R., LaBar, K. S., & Mesulam, M.-M. (2000). Impact of signal-to-noise on functional MRI. *Magnetic Resonance in Medicine*, *44*(6), 925–932. https://doi.org/10.1002/1522-2594(200012)44:6<925::AID-MRM14>3.0.CO;2-M

Petersen, S. E., & Sporns, O. (2015). Brain Networks and Cognitive Architectures. *Neuron*, *88*(1), 207–219. https://doi.org/10.1016/j.neuron.2015.09.027

Pfannmöller, J., & Lotze, M. (2019). Review on biomarkers in the resting-state networks of chronic pain patients. *Brain and Cognition*, *131*, 4–9. https://doi.org/10.1016/j.bandc.2018.06.005

Piché, M., Cohen-Adad, J., Nejad, M. K., Perlbarg, V., Xie, G., Beaudoin, G., Benali, H., & Rainville, P. (2009). Characterization of cardiac-related noise in fMRI of the cervical spinal cord. *Magnetic Resonance Imaging*, *27*(3), 300–310. https://doi.org/10.1016/j.mri.2008.07.019

Pierrot-Deseilligny, E., & Burke, D. (2012). *The Circuitry of the Human Spinal Cord: Spinal and Corticospinal Mechanisms of Movement*. Cambridge University Press.

Pruim, R. H. R., Mennes, M., van Rooij, D., Llera, A., Buitelaar, J. K., & Beckmann, C. F. (2015). ICA-AROMA: A robust ICA-based strategy for removing motion artifacts from fMRI data. *NeuroImage*, *112*, 267–277. https://doi.org/10.1016/j.neuroimage.2015.02.064

Raichle, M. E., MacLeod, A. M., Snyder, A. Z., Powers, W. J., Gusnard, D. A., & Shulman, G. L. (2001). A default mode of brain function. *Proceedings of the National Academy of Sciences*, *98*(2), 676–682. https://doi.org/10.1073/pnas.98.2.676

Ronzano, R., Lancelin, C., Bhumbra, G. S., Brownstone, R. M., & Beato, M. (2021). Proximal and distal spinal neurons innervating multiple synergist and antagonist motor pools. *ELife*, *10*, e70858. https://doi.org/10.7554/eLife.70858

San Emeterio Nateras, O., Yu, F., Muir, E. R., Bazan, C., Franklin, C. G., Li, W., Li, J., Lancaster, J. L., & Duong, T. Q. (2016). Intrinsic Resting-State Functional Connectivity in the Human Spinal Cord at 3.0 T. *Radiology*, *279*(1), 262–268. https://doi.org/10.1148/radiol.2015150768

Sandrini, G., Serrao, M., Rossi, P., Romaniello, A., Cruccu, G., & Willer, J. C. (2005). The lower limb flexion reflex in humans. *Progress in Neurobiology*, *77*(6), 353–395. https://doi.org/10.1016/j.pneurobio.2005.11.003

Särkkä, S., Solin, A., Nummenmaa, A., Vehtari, A., Auranen, T., Vanni, S., & Lin, F.-H. (2012). Dynamic retrospective filtering of physiological noise in BOLD fMRI: DRIFTER. *NeuroImage*, *60*(2), 1517–1527. https://doi.org/10.1016/j.neuroimage.2012.01.067

Schölvinck, M. L., Maier, A., Ye, F. Q., Duyn, J. H., & Leopold, D. A. (2010). Neural basis of global resting-state fMRI activity. Proceedings of the National Academy of Sciences, 107(22), 10238–10243. https://doi.org/10.1073/pnas.0913110107

Sengul, G., Watson, C. R., Tanaka, I., and Paxinos, G. (2013). Atlas of the Spinal Cord: Mouse, Rat, Rhesus, Marmoset, and Human. San Diego: Academic Press.

Sengupta, A., Mishra, A., Wang, F., Li, M., Yang, P.-F., Chen, L. M., & Gore, J. C. (2021). Functional networks in non-human primate spinal cord and the effects of injury. NeuroImage, 240, 118391. https://doi.org/10.1016/j.neuroimage.2021.118391

Shaffer, F., & Ginsberg, J. P. (2017). An Overview of Heart Rate Variability Metrics and Norms. Frontiers in Public Health, 5. https://www.frontiersin.org/articles/10.3389/fpubh.2017.00258

Shehzad, Z., Kelly, A. M. C., Reiss, P. T., Gee, D. G., Gotimer, K., Uddin, L. Q., Lee, S. H., Margulies, D. S., Roy, A. K., Biswal, B. B., Petkova, E., Castellanos, F. X., & Milham, M. P. (2009). The resting brain: Unconstrained yet reliable. *Cerebral Cortex (New York, N.Y.: 1991)*, *19*(10), 2209–2229. https://doi.org/10.1093/cercor/bhn256

Shirer, W. R., Jiang, H., Price, C. M., Ng, B., & Greicius, M. D. (2015). Optimization of rs-fMRI Pre-processing for Enhanced Signal-Noise Separation, Test-Retest Reliability, and Group Discrimination. *NeuroImage*, *117*, 67–79. https://doi.org/10.1016/j.neuroimage.2015.05.015

Shrout, P. E., & Fleiss, J. L. (1979). Intraclass correlations: Uses in assessing rater reliability. *Psychological Bulletin*, *86*(2), 420–428. https://doi.org/10.1037//0033-2909.86.2.420

Shrout, P. E., & Lane, S. P. (2012). Reliability. In H. Cooper, P. M. Camic, D. L. Long, A. T. Panter, D. Rindskopf, & K. J. Sher (Eds.), *APA handbook of research methods in psychology, Vol. 1. Foundations, planning, measures, and psychometrics* (pp. 643–660). American Psychological Association. https://doi.org/10.1037/13619-034

Smyser, C. D., Snyder, A. Z., & Neil, J. J. (2011). Functional connectivity MRI in infants: Exploration of the functional organization of the developing brain. *NeuroImage*, *56*(3), 1437–1452. https://doi.org/10.1016/j.neuroimage.2011.02.073

Stepien, A. E., Tripodi, M., & Arber, S. (2010). Monosynaptic rabies virus reveals premotor network organization and synaptic specificity of cholinergic partition cells. *Neuron*, *68*(3), 456–472. https://doi.org/10.1016/j.neuron.2010.10.019

Triantafyllou, C., Hoge, R. D., Krueger, G., Wiggins, C. J., Potthast, A., Wiggins, G. C., & Wald, L. L. (2005). Comparison of physiological noise at 1.5 T, 3 T and 7 T and optimization of fMRI acquisition parameters. *NeuroImage*, *26*(1), 243–250. https://doi.org/10.1016/j.neuroimage.2005.01.007

Triantafyllou, C., Polimeni, J. R., & Wald, L. L. (2011). Physiological noise and signal-to-noise ratio in fMRI with multi-channel array coils. *NeuroImage*, *55*(2), 597–606. https://doi.org/10.1016/j.neuroimage.2010.11.084

Vahdat, S., Khatibi, A., Lungu, O., Finsterbusch, J., Büchel, C., Cohen-Adad, J., Marchand-Pauvert, V., & Doyon, J. (2020). Resting-state brain and spinal cord networks in humans are functionally integrated. *PLOS Biology*, *18*(7), e3000789. https://doi.org/10.1371/journal.pbio.3000789

Veraart, J., Fieremans, E., & Novikov, D. S. (2016a). Diffusion MRI noise mapping using random matrix theory. *Magnetic Resonance in Medicine*, *76*(5), 1582–1593. https://doi.org/10.1002/mrm.26059

Veraart, J., Novikov, D. S., Christiaens, D., Ades-Aron, B., Sijbers, J., & Fieremans, E. (2016b). Denoising of diffusion MRI using random matrix theory. *NeuroImage*, *142*, 394–406. https://doi.org/10.1016/j.neuroimage.2016.08.016

Verma, T., & Cohen-Adad, J. (2014). Effect of respiration on the B0 field in the human spinal cord at 3T. *Magnetic Resonance in Medicine*, *72*(6), 1629–1636. https://doi.org/10.1002/mrm.25075

Vizioli, L., Moeller, S., Dowdle, L., Akçakaya, M., De Martino, F., Yacoub, E., & Uğurbil, K. (2021). Lowering the thermal noise barrier in functional brain mapping with magnetic resonance imaging. *Nature Communications*, *12*(1), Article 1. https://doi.org/10.1038/s41467-021-25431-8

Watson, C., & Sidhu, A. (2009). Chapter 17—Toward a Spinal Cord Ontology. In C. Watson, G. Paxinos, & G. Kayalioglu (Eds.), The Spinal Cord (pp. 380–383). Academic Press. https://doi.org/10.1016/B978-0-12-374247-6.50021-3

Weber, K. A., Sentis, A. I., Bernadel-Huey, O. N., Chen, Y., Wang, X., Parrish, T. B., & Mackey, S. (2018). Thermal Stimulation Alters Cervical Spinal Cord Functional Connectivity in Humans. *Neuroscience*, *369*, 40–50. https://doi.org/10.1016/j.neuroscience.2017.10.035

Wei, P., Li, J., Gao, F., Ye, D., Zhong, Q., & Liu, S. (2009). Resting state networks in human cervical spinal cord observed with fMRI. *European Journal of Applied Physiology*, *108*(2), 265. https://doi.org/10.1007/s00421-009-1205-4

Wenger, E., Polk, S. E., Kleemeyer, M. M., Weiskopf, N., Bodammer, N. C., Lindenberger, U., & Brandmaier, A. M. (2022). Reliability of quantitative multiparameter maps is high for magnetization transfer and proton density but attenuated for R_1 and R_2* in healthy young adults. *Human Brain Mapping*, *43*(11), 3585–3603. https://doi.org/10.1002/hbm.25870

Wig, G. S. (2017). Segregated Systems of Human Brain Networks. *Trends in Cognitive Sciences*, *21*(12), 981–996. https://doi.org/10.1016/j.tics.2017.09.006

Winkler, A. M., Ridgway, G. R., Webster, M. A., Smith, S. M., & Nichols, T. E. (2014). Permutation inference for the general linear model. *NeuroImage*, *92*, 381–397. https://doi.org/10.1016/j.neuroimage.2014.01.060

Woolrich, M. W., Ripley, B. D., Brady, M., & Smith, S. M. (2001). Temporal Autocorrelation in Univariate Linear Modeling of FMRI Data. *NeuroImage*, *14*(6), 1370–1386. https://doi.org/10.1006/nimg.2001.0931

Wu, T., Wang, F., Mishra, A., Wilson, G. H., Byun, N., Chen, L. M., & Gore, J. C. (2018). Resting-state functional connectivity in the rat cervical spinal cord at 9.4 T. *Magnetic Resonance in Medicine*, *79*(5), 2773–2783. https://doi.org/10.1002/mrm.26905

Wu, T.-L., Yang, P.-F., Wang, F., Shi, Z., Mishra, A., Wu, R., Chen, L. M., & Gore, J. C. (2019). Intrinsic functional architecture of the non-human primate spinal cord derived from fMRI and electrophysiology. *Nature Communications*, *10*(1), Article 1. https://doi.org/10.1038/s41467-019-09485-3

Zou, Q., Miao, X., Liu, D., Wang, D. J. J., Zhuo, Y., & Gao, J.-H. (2015). Reliability comparison of spontaneous brain activities between BOLD and CBF contrasts in eyes-open and eyes-closed resting states. *NeuroImage*, *121*, 91–105. https://doi.org/10.1016/j.neuroimage.2015.07.044

Supplementary Material

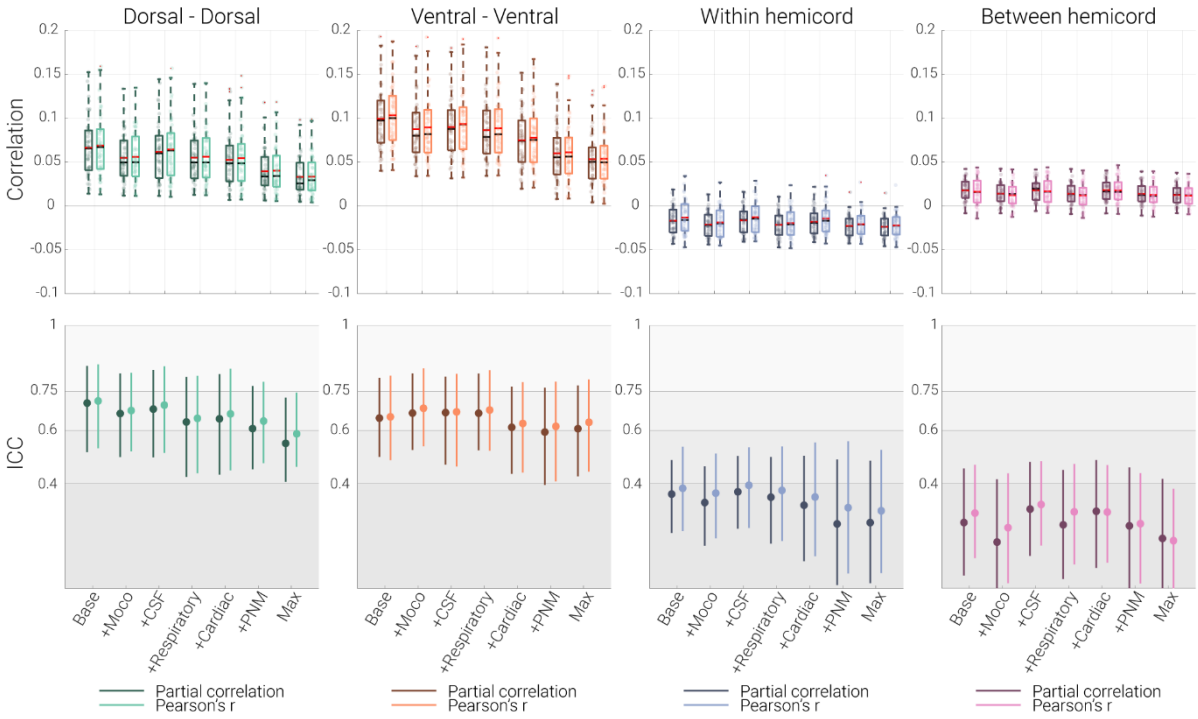

Figure S1. **Partial correlation vs Pearson correlation**. The top panels depict functional connectivity estimates between different ROIs calculated with either partial correlation or Pearson correlation (average across two sessions) using grouped box plots for the seven denoising pipelines. For the box plots, median and mean are denoted by the central black and red marks, respectively. The bottom and top edges of the boxes represent the 25th and 75th percentiles, respectively, with the whiskers encompassing ~99% of the data, and the outliers being denoted with red dots. The bottom panels depict ICC values for different denoising pipelines with dots and lines denote 95% confidence intervals. The gray scale background reflects the ICC ranges (as defined by Cicchetti & Sparrow (1981) and Hallgren (2012)): poor <0.4, fair 0.4–0.59, good 0.6–0.74, excellent ≥0.75.

Table S1. *Functional connectivity and its reliability after addition of pre-whitening to the maximal denoising pipeline.*

	Dorsal Dorsal	**Ventral Ventral**	**Within Hemicord**	**Between Hemicord**
Maximal	r = 0.03 t = 9.5 p < 0.001 ICC (95% CI) = 0.59 (0.46 – 0.74)	r = 0.05 t = 11.6 p < 0.001 ICC (95% CI) = 0.63 (0.44 – 0.79)	r = -0.02 t = -10.7 p < 0.001 ICC (95% CI) = 0.30 (0.06 – 0.53)	r = 0.01 t = 6.7 p < 0.001 ICC (95% CI) = 0.18 (-0.03 – 0.38)
Maximal + Pre-whitening	r = 0.03 t = 9.6 p < 0.001 ICC (95% CI) = 0.59 (0.46 – 0.74)	r = 0.05 t = 11.7 p < 0.001 ICC (95% CI) = 0.65 (0.47 – 0.80)	r = -0.02 t = -10.6 p < 0.001 ICC (95% CI) = 0.29 (0.06 – 0.52)	r = 0.01 t = 6.7 p < 0.001 ICC (95% CI) = 0.17 (-0.05 – 0.37)

This table depicts functional connectivity and reliability results of each connection for two processing pipelines: the maximal pipeline and the maximal pipeline with the inclusion of FILM pre-whitening. r represents the mean Pearson correlation across participants, t and p represent the t-value and two-tailed family-wise-error corrected p-value from a permutation test (against 0), respectively. ICC (95% CI) represents ICC(2,1) values and 95% bootstrapped confidence intervals.

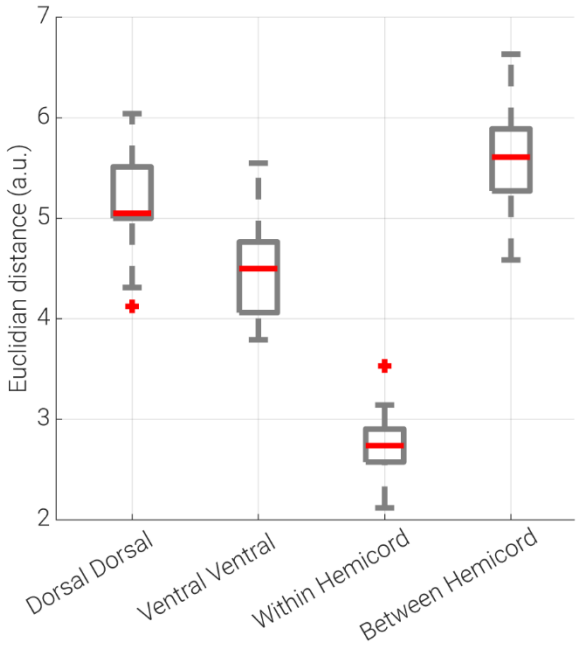

Figure S2. **Euclidian distance between ROIs**. Box plots show the median Euclidian distance between the closest voxels of different ROIs (within each slice) across slices and participants. The median is denoted by the central red line. The bottom and top edges of the boxes represent the 25th and 75th percentiles, respectively, with the whiskers encompassing ~99% of the data, and the outliers are denoted with the red crosses.